POLITECNICO DI TORINO
Repository ISTITUZIONALE

Manipulation of a turbulent boundary layer using sinusoidal riblets

Original
Manipulation of a turbulent boundary layer using sinusoidal riblets / Cafiero, G., Amico, E., Iuso, G.. - In: JOURNAL OF FLUID MECHANICS. - ISSN 0022-1120. - 984:(2024). [10.1017/jfm.2024.256]

Availability:
This version is available at: 11583/2987685 since: 2024-04-09T14:21:03Z

Publisher:
cambridge university press

Published
DOI:10.1017/jfm.2024.256

Terms of use:

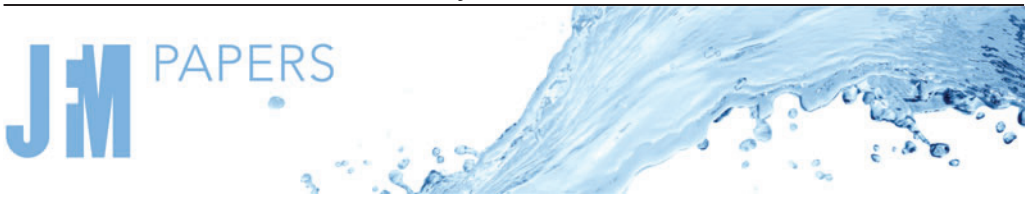
This article is made available under terms and conditions as specified in the corresponding bibliographic description in the repository

Publisher copyright

(Article begins on next page)

27 November 2026

J. Fluid Mech. (2024), *vol*. 984, A59, doi:10.1017/jfm.2024.256



Manipulation of a turbulent boundary layer using sinusoidal riblets

Gioacchino Cafiero[1],†, **Enrico Amico**[1] **and Gaetano Iuso**[1]

[1]Department of Mechanical and Aerospace Engineering, Politecnico di Torino, Corso Duca degli Abruzzi 24, 10129, Turin, Italy

(Received 28 July 2023; revised 29 February 2024; accepted 1 March 2024)

We investigate experimentally the effects of micro-grooves on the development of a zero pressure gradient turbulent boundary layer at two different values of the friction Reynolds number. We consider both the well-known streamwise aligned riblets as well as wavy riblets, characterized by a sinusoidal pattern in the mean flow direction. Previous investigations by the authors showed that sinusoidal riblets yield larger values of drag reduction with respect to the streamwise aligned ones. We perform new particle image velocimetry experiments on wall-parallel planes to get insights into the effect of the sinusoidal shape on the near-wall organisation of the boundary layer and the structures responsible for the friction drag reduction and the turbulence generation. Conditional averages, aimed at identifying the topology of the low-speed streaks in the turbulent boundary layer, reveal that the flow is highly susceptible to wall manipulation. This is particularly evident in the cases that are associated with greater values of drag reduction. The results suggest a fragmentation and/or weakening of the streaks in the sinusoidal cases, that is triggered by the larger values of the wall-normal vorticity found at the streaks' edges. The results are also confirmed by applying the variable interval spatial averaging events eduction technique. The turbulent kinetic energy budget also shows that the sinusoidal geometry significantly attenuates the turbulence production, hence supporting the idea of the manipulation of the turbulence regeneration cycle.

Key words: turbulent boundary layers, drag reduction

1. Introduction

The definition of effective drag reduction techniques covers a key role to meet the ambitious targets of reducing the pollution of the transportation sector. In the aeronautical

† Email address for correspondence: gioacchino.cafiero@polito.it

© The Author(s), 2024. Published by Cambridge University Press. This is an Open Access article, distributed under the terms of the Creative Commons Attribution-NonCommercial-NoDerivatives licence (http://creativecommons.org/licenses/by-nc-nd/4.0), which permits non-commercial re-use, distribution, and reproduction in any medium, provided that no alterations are made and the original article is properly cited. The written permission of Cambridge University Press must be obtained prior to any commercial use and/or adaptation of the article.

https://doi.org/10.1017/jfm.2024.256 Published online by Cambridge University Press

sector, for instance, the skin friction drag may be as large as 50 % of the overall drag count. The skin friction is intimately related to the turbulent structures that populate the inner layer of a turbulent boundary layer. A rather general consensus has been reached on the existence of a self-sustained cycle that leads to the regeneration of these turbulence structures.

Jiménez & Pinelli (1999) described an autonomous cycle for the regeneration mechanism in wall-bounded turbulent flows. An extensive review on this topic is due to Panton (2001). Coherent structures and organized motions are the main players in a turbulent boundary layer, as they drive the dynamics of the wall turbulence. Low- and high-speed streaks in addition to quasi-streamwise vortices populate the near-wall region, as reported by many authors (Schoppa & Hussain 2000, 2002). Moreover, other coherent structures develop from the near-wall region to the outer part of the boundary layer such as hairpin vortices, which are generally found in packets, as shown by Zhou *et al.* (1999), Adrian, Meinhart & Tomkins (2000) and Ganapathisubramani, Longmire & Marusic (2003); very long meandering superstructures characterized by streamwise velocity fluctuations have also been evidenced in a turbulent boundary layer by Hutchins & Marusic (2007).

Elongated streaks characterized by positive and negative values of the streamwise velocity fluctuations represent structures with a streamwise correlation length that is significantly larger than their cross-stream correlation length. Kline *et al.* (1967) and Lu & Willmarth (1973) conjectured that the streaks are dominant contributors to the cross-stream transfer of momentum and to the generation of turbulence drag. The self-sustaining cycle is associated with the self-generation mechanism of these structures in a turbulent boundary layer (Jiménez 2022).

The interruption of this self-sustained cycle leads to the suppression of the exchange of momentum between the outer and inner regions of the boundary layer, and as such to the reduction of the turbulent fluxes near the wall, in turn promoting an attenuation of the skin friction drag.

The definition of efficient flow control techniques to reduce skin friction drag has represented one of the main objectives of the scientific community interested in flow control. Passive methodologies, i.e. not requiring any power supplied to the system, have shown interesting results both in boundary layers (Iuso & Onorato 1995; Sirovich & Karlsson 1997; Corke & Thomas 2018) as well as to reduce the induced drag (Gehlert *et al.* 2021) or increase the convective heat transfer and the entrainment rate of impinging jets (Cafiero *et al.* 2019; Cafiero, Castrillo & Astarita 2021), to cite some other examples.

Active solutions, on the other hand, require a dedicated power supply but can achieve significantly larger values of drag reduction. One of the most efficient techniques in the attenuation of wall turbulence (drag reduction and turbulence intensity) employs the spanwise oscillation of the wall (Choi 2002; Di Cicca *et al.* 2002*a*; Quadrio & Ricco 2004; Touber & Leschziner 2012; Gatti & Quadrio 2016; Marusic *et al.* 2021; Ricco, Skote & Leschziner 2021; Chandran *et al.* 2023; Rouhi *et al.* 2023) or the formation of transverse (Du, Symeonidis & Karniadakis 2002) or streamwise (Hurst, Yang & Chung 2014) oriented travelling waves. Large-scale forcing aimed at the manipulation of the wall turbulence for skin friction drag reduction has also shown encouraging results (Schoppa & Hussain 1998; Di Cicca *et al.* 2002*b*; Iuso *et al.* 2002; Yao, Chen & Hussain 2018; Cannata, Cafiero & Iuso 2020; Chan *et al.* 2021; Cheng *et al.* 2021).

One of the most promising passive solutions that have been proposed in the past is providing permanent geometry manipulations to the wall, through micro-grooves. These grooves are generally referred to as riblets (Walsh 1980, 1982, 1983; Vukoslavcevic,

https://doi.org/10.1017/jfm.2024.256 Published online by Cambridge University Press

Wallace & Balint 1992; Viswanath 2002; Garcia-Mayoral & Jimenez 2012; Endrikat *et al.* 2021, 2022; Ran, Zare & Jovanović 2021; Rouhi *et al.* 2022; Von Deyn, Gatti & Frohnapfel 2022; Malathi Ananth *et al.* 2023; Zhang, Cai & Li 2024).

The key parameters of the riblet geometry are the depth of the micro-groove, the spacing between the grooves, and the groove cross-section. An extensive parametric study carried out by Bechert *et al.* (1997) has shown that blade riblets aligned to the streamwise direction yield the highest drag reduction, but parabolic-shaped profiles could respond better to the ease of manufacturing for realistic application.

A non-dimensional riblet spacing ($s^+ = su_\tau/\nu$, with u_τ being the friction velocity and ν the kinematic viscosity, and the superscript $+$ indicating the scaling in inner units) of approximately 15–16 demonstrated the highest values of drag reduction. More recently, García-Mayoral & Jiménez (2011) introduced a dimensionless parameter $l_g^+ = (A_g^+)^{1/2}$, accounting for the cross-sectional area (A_g^+) of the riblet profile. The authors showed that the highest drag reduction would be obtained for $l_g^+ \approx 11$.

The underlying mechanism leading to drag reduction associated with riblet surfaces has been addressed in the literature via experimental investigations (Choi 1989), theoretical analyses (Luchini, Manzo & Pozzi 1991; Wong *et al.* 2024) and numerical simulations (Choi, Moin & Kim 1993; Mele & Tognaccini 2018; Mele *et al.* 2020), among others. The authors showed that the optimal value of the spacing corresponds to the condition where the near-wall structures cannot fit within the groove; hence the structures are displaced towards the outer layers of the boundary layer. Near the wall, a region of nearly stagnating flow is then produced, with a corresponding reduction of the wall shear stress and skin friction drag.

More recently, sinusoidal riblets (also referred to as wavy riblets) have been proposed as an alternative solution that could join the benefits of straight riblets with the spanwise-induced motion of the wall oscillation (Peet, Sagaut & Charron 2008; Peet & Sagaut 2009; Kramer *et al.* 2010; Grüneberger *et al.* 2012; Sasamori, Iwamoto & Murata 2012; Sasamori *et al.* 2014, 2017; Okabayashi 2016; Mamori *et al.* 2019; Cafiero & Iuso 2022). Starting from the theoretical and numerical work by Peet & Sagaut (2009), which showed that the sinusoidal riblets could cater for an added share of friction drag reduction as large as 50 % of the straight riblets, a large body of work has been performed on validating these results experimentally and numerically. Grüneberger *et al.* (2012) investigated experimentally a turbulent channel flow manipulated with sinusoidal riblets, considering a range of amplitudes and wavelengths. Their results did not show the same beneficial effects demonstrated by the large-eddy simulations of Peet *et al.* (2008), possibly owing to the limited streamwise extent of the surface manipulation, which did not provide a sufficient distance for the onset of the drag reduction. Mamori *et al.* (2019) performed measurements on sinusoidal riblets with varying lateral spacing in a turbulent channel flow at friction Reynolds number 150, attaining values of drag reduction close to 12 %.

In their recent investigation, Cafiero & Iuso (2022) demonstrated experimentally that sinusoidal riblets in a turbulent boundary layer at a friction Reynolds number of nearly 1200 cater for values of drag reduction as large as 10 %, with an enhancement of about 3 % when compared with straight riblets. The results were obtained through direct friction drag measurements, planar and stereoscopic particle image velocimetry (PIV) carried out in the streamwise wall-normal plane, and hot-wire anemometry. The results were supported by a general attenuation of the variance of the streamwise velocity across the buffer layer, with a corresponding enhancement of the spanwise-induced motion as elucidated via variable integral spatial averaging (VISA) of the spanwise velocity, measured via stereoscopic PIV. Nevertheless, several aspects remained unexplored for a more exhaustive comprehension

https://doi.org/10.1017/jfm.2024.256 Published online by Cambridge University Press

of the near-wall flow structure modifications leading to the friction drag attenuation. This is the scope of the present investigation: to provide insights into how the sinusoidal riblets manipulate the low-speed streaks (LSS). Evidence has been provided in the literature on how the streaky structures influence the wall shear stress. Orlandi & Jiménez (1994) have shown numerically and analytically that the average wall friction is increased by the formation of the streaks in a turbulent boundary layer. As mentioned already, the drag reduction evidenced in the previous experimental investigation is expected to be associated with a modification of the self-sustaining production of the near-wall turbulence. In this paper, we show through wall-parallel PIV experiments that sinusoidal riblets have a striking effect on the LSS, and that this effect becomes more significant in conditions where the drag reduction is larger. This work builds on the results obtained by Cafiero & Iuso (2022), and provides new insights on the flow organization by performing new experiments that are tailored to best highlight the manipulation of the near-wall flow structures. It is therefore worth mentioning explicitly the results that are taken from the previous experimental dataset, namely: (i) the value of the friction velocity for all the investigated cases, which are obtained by applying a Clauser fit to the logarithmic portion of the mean flow velocity profile; (ii) the values of the drag reduction obtained from the direct load cell measurements; (iii) the wall-normal turbulence production profile, measured via PIV experiments carried out in the streamwise/wall-normal plane.

The paper is organized as follows. In § 2, we provide a description of the experimental apparatus and the measurement techniques. In § 3, we report the main findings obtained through the statistical analysis of the PIV data. Finally, we draw our conclusions in § 4.

2. Experimental apparatus

The experiments were performed in an open circuit wind tunnel at Politecnico di Torino. The tunnel has a settling chamber containing honeycomb and mesh screens, followed by a contraction with area ratio 3 : 1, leading into a test section that is 5300 mm long, with cross-section 500×700 mm^2.

The flat plate where the boundary layer develops is located at mid-height of the test section and extends from side to side, thus effectively reducing the cross-sectional area to 500×350 mm^2. This reduction is obtained through a contoured contraction. The purpose of this is twofold. First, it avoids sharp area variations, which would disrupt the quality of the flow. Second, it allows for the insulation of the bottom portion of the test section which is used for the plate positioning system. A trip wire is placed at the start of the flat plate to trigger an early transition to a turbulent boundary layer.

A portion of the flat plate of size 260×260 mm^2 is hollow, allowing the insertion of different plates. The correct alignment of the tested plate with respect to the remaining portion of the flat plate is ensured with micrometric accuracy through the possibility of controlling the height and the inclination of the tested plate. In particular, the height is controlled using a laser optical displacement measurement optoNCDT 1320 manufactured by Micro-Epsilon, whilst the inclination is checked through a high-precision inertial unit.

The alignment of the mounting plate to the surroundings is performed through the combination of the high-precision laser and a calibrated glass. The vertical positioning of each riblet plate is changed with micrometric accuracy using a stepper motor. The plate is considered aligned when it touches the calibrated glass. The reading of the laser displacement measurement is considered as the datum. The reasoning behind this choice is twofold. First, it allows us to provide a more accurate alignment of the removable plate with the surroundings. Second, as shown by Malathi Ananth *et al.* (2023), the abrupt change

https://doi.org/10.1017/jfm.2024.256 Published online by Cambridge University Press

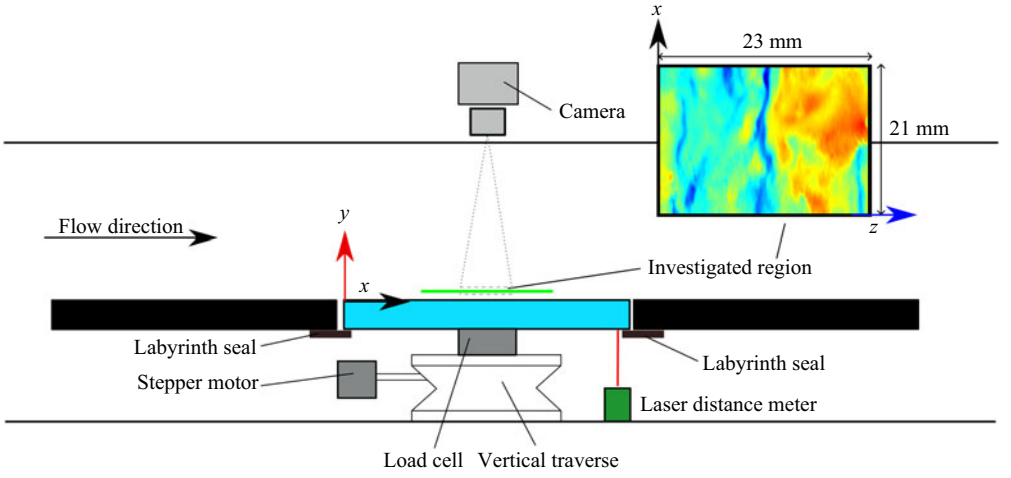


Figure 1. Schematic representation of the test section with detail of the removable plate. The track of the laser sheet, indicated in green, is not to scale. The inset reports a representative snapshot with the indication of the streamwise and spanwise extents of the measurement region.

in the wall roughness leads to the formation of coherent spanwise structures originating at the riblets region leading edge.

Four different plates were investigated: a flat plate (Smooth), a riblet plate with longitudinal grooves (RLong), and two riblet plates with sinusoidal grooves (RS1 and RS2). Each of the tested plates is a square of side 258 mm and thickness 10 mm. This leads to a small gap between the edge of the tested plate and the flat plate. A labyrinth seal was mounted underneath the plate to avoid any leakage through the gap between the tested plate and the flat plate.

The three riblet plates are characterized by the same groove profile of parabolic shape. The height of the groove is $h = 210$ µm, whilst the spacing between two grooves is $s = 300$ µm, resulting in a h/s ratio equal to 0.7 (see figure 2*a*). The two sinusoidal riblets are characterized by the same wavelength $\lambda = 19.2$ mm, thus leading to at least $N_\lambda = 13$ wavelengths on the tested plate; conversely, two different values of the amplitude a are considered (see figure 2*b*), with $a = 0.15$ mm in RS1 and $a = 0.6$ mm in RS2, respectively. A summary of the geometric parameters of the riblet plates is reported in table 1.

The riblet performance is strongly dependent on the spacing in inner units $s^+ = s/l_\tau$, where $l_\tau = \nu/u_\tau$ is the viscous length scale, ν is the air kinematic viscosity, and u_τ is the friction velocity. Since the manufacturing of the riblet plates can be expensive, we vary s^+ by changing the Reynolds number.

The freestream speed U_∞ is measured using a Pitot tube located at the inlet of the test section and connected to a pressure transducer Setra 239C having a full scale of ± 0.2 psi and ± 0.14 % accuracy.

Two different inlet conditions are investigated, corresponding to values of the Reynolds number based on the momentum thickness θ ($Re_\theta = U_\infty \theta/\nu$) equal to 2200 and 2900, respectively. Details of the experimental conditions are listed in table 2. The values of the friction velocity u_τ were obtained in a previous investigation via hot-wire measurements (Cafiero & Iuso 2022) carried out at the centre of each plate and applying a Clauser fit to the logarithmic portion of the mean flow profile. The values of the constants $k = 0.41$ and $B = 5.2$ were selected using those suggested by Pope (2000), which were then verified

https://doi.org/10.1017/jfm.2024.256 Published online by Cambridge University Press

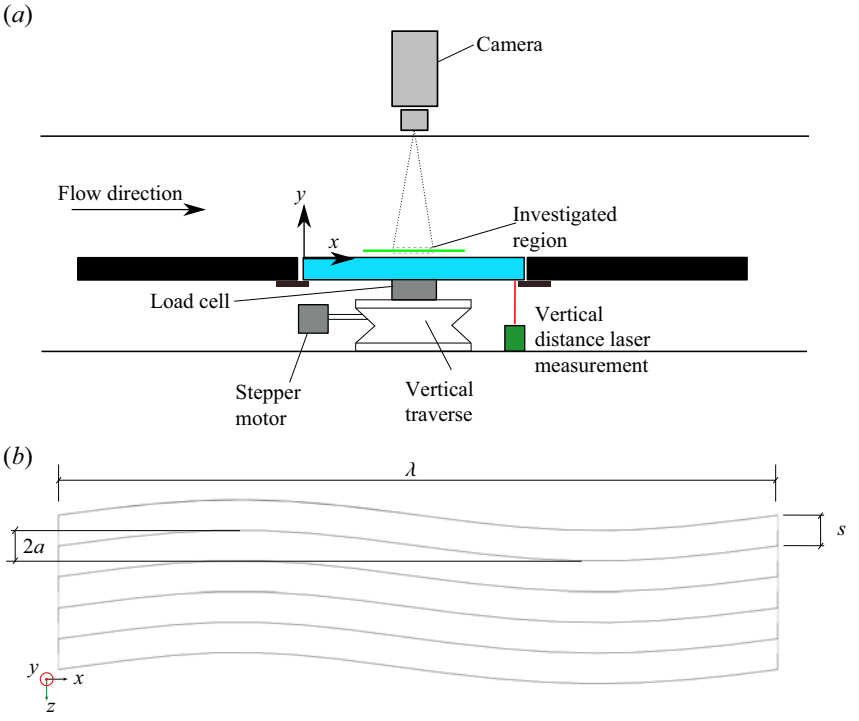


Figure 2. Detail of the parabolic profile of the grooves: (*a*) isometric view, and (*b*) top view. One wavelength λ is represented in the figure for the sake of clarity.

	RLong	RS1	RS2
s (mm)	0.30	0.30	0.30
h (mm)	0.21	0.21	0.21
h/s	0.70	0.70	0.70
a (mm)	0	0.15	0.60
λ (mm)	∞	19.2	19.2
N_λ	N.A.	13	13

Table 1. Geometric data for the micro-grooves.

U_∞ (m s^{-1})	u_τ^S (m s^{-1})	Re_τ	Re_θ	δ (mm)	l_τ (μm)	H	s^+	λ^+	a^+_{RS1}	a^+_{RS2}
8.30	0.36	1050	2200	44.9	42.5	1.36	7.06	451	3.53	14.1
13.4	0.53	1210	2900	34.5	28.4	1.34	10.6	676	5.28	21.1

Table 2. Experiment details: values of the asymptotic speed U_∞, friction velocity u_τ^S of the Smooth case, Reynolds numbers based on friction velocity (Re_τ) and momentum thickness (Re_θ), boundary layer thickness δ, viscous length scale l_τ, and boundary layer shape factor H. The values of the spacing s^+, wavelength of the groove λ^+ and amplitude of the sinusoidal profile a^+ are normalized in inner units using the Smooth case data.

on the experimental data obtained via hot-wire anemometry. The obtained values of the friction velocity for each of the investigated plates is then used to normalize the flow quantities in inner units. It is also worth mentioning explicitly that the effect of a change in the value of k on the resulting value of u_τ was investigated. This is due to the potential

https://doi.org/10.1017/jfm.2024.256 Published online by Cambridge University Press

Re_θ	s^+	RLong	RS1	RS2
2200	7.06	−5.0	−4.8	−5.2
2900	10.6	−5.9	−7.9	−8.5

Table 3. Percentage drag reduction ($100 \times (D - D^S)/D^S$) obtained at the two investigated values of s^+, 7.06 and 10.6. Here, D indicates the drag measured for the manipulated cases, while D^S indicates the drag measured for the Smooth case.

changes on the values of the log law associated with a manipulated boundary layer (Skote 2012, 2013, 2014). By varying the value of k in the range between 0.38 and 0.41, and applying the Clauser fit to the mean flow profile in the manipulated cases, the resulting change in u_τ is less than 3 %. Therefore, we deemed it reasonable to utilize the Clauser fit (with the values $k = 0.41$ and $B = 5.2$) to determine the value of the friction velocity also for the manipulated cases.

The two investigated conditions correspond to different behaviours of the riblets (Cafiero & Iuso 2022): one condition with a value of drag reduction similar to that in the RLong case (at $s^+ = 7.06$), and one condition close to the maximum drag reduction (at $s^+ = 10.6$). The drag values were measured using a load cell, which yielded the global value of the friction drag on the sensing plate. The corresponding values of the drag reduction are reported in table 3.

The spatial organization of the flow was investigated through low-speed planar PIV in planes parallel to the wall (x–z plane). A Dantec Dynamics Nd:YAG Dual Power 200 laser (200 mJ pulse^{-1} energy, 15 Hz repetition rate) operated in dual pulse mode was used to illuminate the tracing particles. The laser beam was shaped into a thin sheet of less than 1 mm thickness using a combination of spherical and cylindrical lenses. The final thickness was refined further using a mask connected to the wind tunnel wall. The illuminated region was centred with respect to the removable plate, as indicated schematically in figure 1.

One Andor Zyla 5.5 Mpixel sCMOS camera (sensor size 2560 × 2160 pixel, pixel size 6.5μm) was used to capture the images of the tracing particles. The camera was equipped with a Nikkor 200 mm Micro lens, operated at a value of the aperture $f_\# = 11$. The acquisition frequency was set to 15 Hz. The imaged area extended for 21 mm in the streamwise direction (x) and 23 mm in the cross-stream direction (z). The corresponding value of the digital resolution was approximately 93 pixel mm^{-1}.

The flow was seeded upstream of the stagnation chamber using HAZEBASE Base M Fog Fluid. The small droplets of diameter 1 μm were generated using a SAFEX Fog generator. For each Reynolds number and each plate, 2000 pairs of images were acquired. The raw images were pre-processed using a proper orthogonal decomposition approach to reduce to a minimum the spurious reflection within the illuminated region (Mendez *et al.* 2017).

The vector fields were obtained by processing the collected images using a correlation-based algorithm. A spline interpolation of the image and of the velocity field was performed, as recommended by Astarita (2006, 2008). A Blackman weighting window was used to tune the spatial resolution (Astarita 2007). The algorithm is based on a multi-pass approach, and the final interrogation window size was 48 × 48 pixel, with 75 % overlap. The resulting vector spacing is approximately $3.03l_\tau$ at $Re_\theta = 2200$ and $4.54l_\tau$ at $Re_\theta = 2900$.

https://doi.org/10.1017/jfm.2024.256 Published online by Cambridge University Press

3. Results

3.1. *Manipulation of the LSS*

The wall-parallel PIV data allowed the investigation of how the surface roughness manipulates the turbulent structures that are typical of the boundary layer. In particular, the focus of this investigation was the analysis of the LSS.

The first step of the investigation was concerned with the detection of the LSS. It is worth mentioning that for the high-speed streaks, a similar procedure can be applied.

The detection of the LSS was based on the definition of a threshold on the local value of the streamwise velocity, as suggested by Iuso *et al.* (2003) and Schoppa & Hussain (2002). Regions of streamwise fluctuating velocity $u(x_i, z_i) < -u_{thr}$ are first identified in the image. For the present investigation, $u_{thr} = 0.5u_\tau$. Within each identified region, the (x_c, z_c) locations of local minima of u in z are identified as streak centres. The z positions where u exhibits a zero-crossing are recognized as the streak borders. Furthermore, the spanwise distance between the centroids of the two closest LSS detected within a snapshot is defined as the streaks' spacing λ_z. The procedure is then repeated for all the streaks educed from each snapshot.

Different approaches were also tested, such as the one described by Lin *et al.* (2008) based on the ratio between the mean and the standard deviation of the streamwise velocity, which led to similar results.

As evidenced in previous investigations (Choi 2002; Iuso *et al.* 2003; Quadrio & Ricco 2004; Ricco 2004; Yao, Chen & Hussain 2019), active flow control techniques such as the spanwise oscillation of the wall can lead to significant variations in the statistical distribution of the near wall streaks. Variations are also expected in the present investigations, although more limited due to the fact that the control technique is passive, and as such, it yields much lower values of drag reduction.

Following the eduction approach described above, the streaks' spacing λ_z and their width w_S are analysed initially. A statistical description of the two parameters, streaks' spacing (λ_z^+) and width (w_S^+), is instrumental to determine the effect of the wall manipulation on the structure of the boundary layer. It is worth mentioning explicitly that the quantities are normalized in inner units using the values of the friction velocity calculated for each case from a Clauser fit applied to the logarithmic region of the mean velocity profile measured by Cafiero & Iuso (2022). In figure 3, the probability density functions (p.d.f.s) of λ_z^+ and w_S^+ obtained from the Smooth, RLong, RS1 and RS2 cases at the two investigated values of Re_θ are reported. At the lowest value of Re_θ, corresponding to $s^+ \approx 7$, the effect of the manipulation is only weakly evidenced on the distributions of the LSS spacing (λ_z^+), as reported in figure 3(*a*). In particular, the effect of the ribbed geometry, regardless of the specific manipulation, is such that larger values of the streaks' spacing are less probable. The peak of the p.d.f., which is found at $\lambda_z^+ \approx 130$ for the Smooth case, shifts towards smaller values at $\lambda_z^+ \approx 110$. The limited variations of the p.d.f. are in good agreement with the direct measurements of the friction drag reported in table 3. Indeed, the RS cases yielded small values of the drag reduction, with similar values attained also with the RLong case.

Similar considerations can also be drawn for the streaks' width (figure 3*b*), at $Re_\theta = 2200$. The main difference in the p.d.f.s can be found in the fact that ribbed geometries yield greater probabilities of streaks width in the range of values between 25 and 45. The p.d.f.s of both spacing and width show a similar behaviour, with a horizontal shift of the curves for all the manipulated cases towards lower values of both λ_z^+ and w_S^+.

https://doi.org/10.1017/jfm.2024.256 Published online by Cambridge University Press

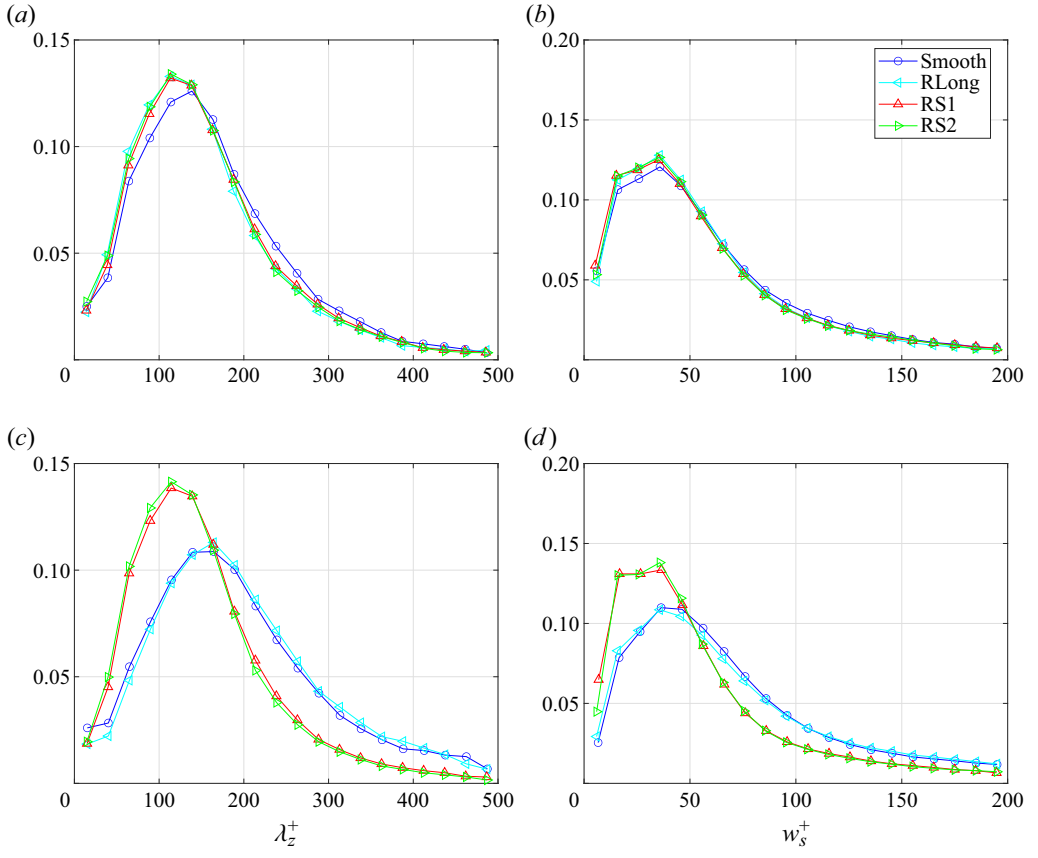


Figure 3. Probability density function of the streaks' (*a*,*c*) spacing and (*b*,*d*) width. Data are collected at (*a*,*b*) $Re_\theta = 2200$ and $y^+ = 35$, (*c*,*d*) $Re_\theta = 2900$ and $y^+ = 50$.

At $Re_\theta = 2900$, corresponding to $s^+ \approx 11$, the sinusoidal riblets were found to be more effective in terms of drag reduction than the longitudinal ones, as documented in table 3. The effectiveness in terms of drag reduction is also reflected in a more prominent manipulation of the LSS.

The p.d.f.s of the streaks' spacing are reported in figure 3(*c*). Both the Smooth and RLong cases show a peak at $\lambda_z^+ \approx 110$, which is in good agreement with the literature on the topic. The sinusoidal cases, instead, show a rather different behaviour. The p.d.f. is skewed towards smaller values of λ_z^+, peaking at $\lambda_z^+ \approx 110$. Small differences are instead evidenced between RS1 and RS2 cases. Moreover, the streaks' spacing values greater than $\lambda_z^+ \approx 150$ are less probable in the sinusoidal cases.

The p.d.f.s of the streaks' width obtained at $Re_\theta = 2900$, corresponding to $s^+ \approx 11$, are reported in figure 3(*d*). While the Smooth and RLong cases feature distributions of the width that are not significantly different from those reported in figure 3(*b*), this is not so for the sinusoidal cases. In particular, the p.d.f. exhibits a plateau in the range of w_S^+ between 25 and 45, with a corresponding lower probability of finding streaks with values of w_S^+ greater than 50.

On the basis of the results presented above, a first summary of the effect of the manipulation can be drawn. In the sinusoidal cases, the LSS are closer together and

https://doi.org/10.1017/jfm.2024.256 Published online by Cambridge University Press

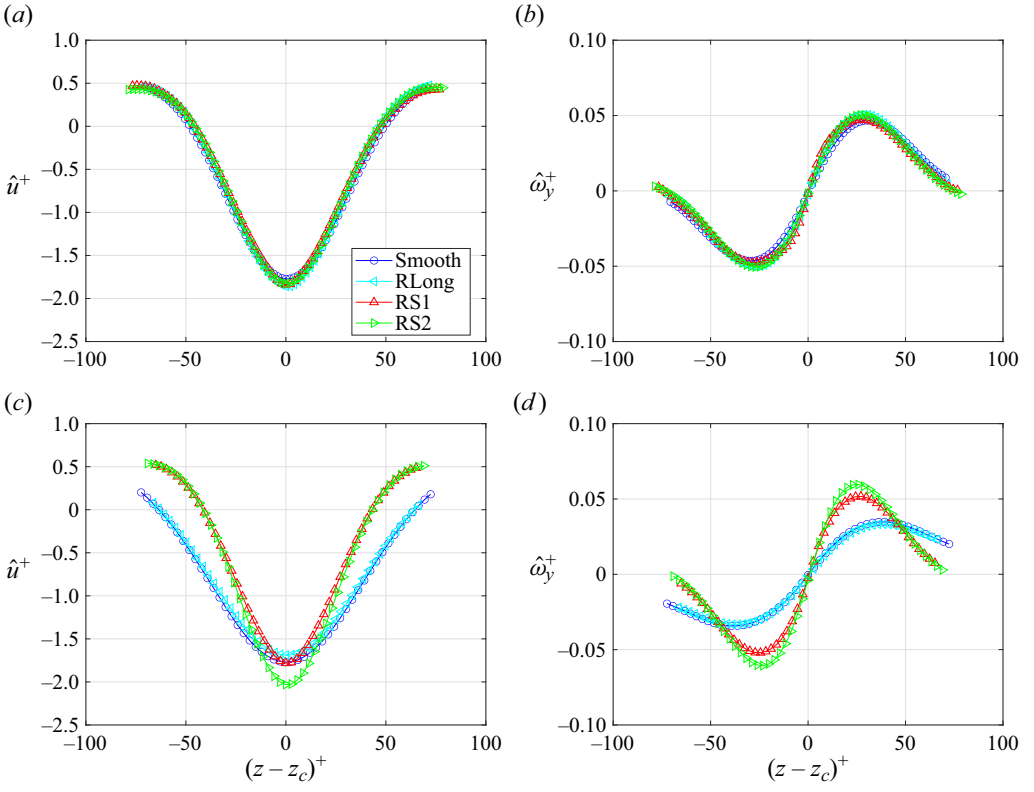


Figure 4. Conditionally averaged (*a*,*c*) streamwise velocity fluctuations and (*b*,*d*) wall-normal vorticity profiles, calculated across the LSS. Data are collected at (*a*,*b*) $Re_\theta = 2200$ and $y^+ = 35$, (*c*,*d*) $Re_\theta = 2900$ and $y^+ = 50$.

thinner. This effect increases at values of s^+ where the RS cases are more effective in reducing drag. This effect will be linked to the drag reduction mechanism later in the paper.

The conditional averages of the mean streamwise velocity and wall-normal vorticity profiles, calculated across the streaks, can provide further evidence of the topology of the streaky structures.

Figure 4 shows the conditionally averaged streamwise velocity fluctuations ($\hat{u}^+$) and wall-normal vorticity ($\hat{\omega}_y^+$) profiles. Starting from the streak's centre (z_c) at all the streamwise locations corresponding to a streak, the streamwise velocity and wall-normal vorticity values in the range $-70 < z - z_c < 70$ are stored and then averaged over all the educed streaks.

The profiles are plotted in a reference frame that is centred on the streak, $(z - z_c)^+$. Here and in the following, the hat symbol will be used to indicate that the average is performed on points belonging to the identified LSS.

At $Re_\theta = 2200$, both the streamwise velocity and the wall-normal vorticity profiles do not show significant differences between the investigated cases. Figure 4(*a*) shows that all cases exhibit a velocity deficit associated with the presence of the LSS, at least concerning RS2. The RS cases are characterized by a narrower profile, attaining a plateau at smaller values of $|(z - z_c)^+|$. The wall-normal vorticity profiles reported in figure 4(*b*) highlight these differences further. The sinusoidal cases are characterized by

https://doi.org/10.1017/jfm.2024.256 Published online by Cambridge University Press

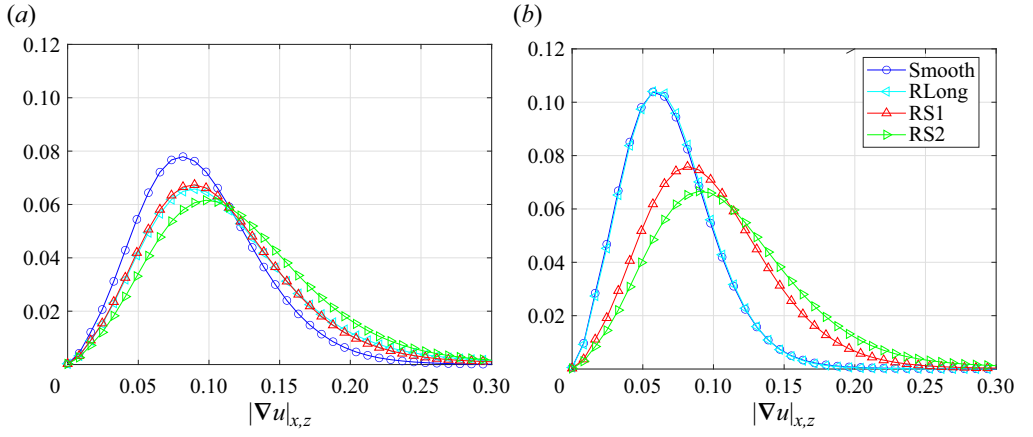


Figure 5. Probability density functions of the modulus of the velocity gradient ($|\nabla \hat{u}|_{x,z}$) projected on the x–z plane calculated at the streaks' edges, for (*a*) $Re_\theta = 2200$ and $y^+ = 35$, (*b*) $Re_\theta = 2900$ and $y^+ = 50$.

a steeper slope of the $\hat{\omega}_y^+$ profile at $(z - z_c)^+ = 0$. Furthermore, even though only limited differences are detectable, the spanwise distance between the peaks is reduced in the RS cases, consistently with results reported in figure 3(*b*). Indeed, this distance can be associated with the typical streaks' width.

At $Re_\theta = 2900$, which corresponds to $s^+ \approx 11$, much clearer differences can be detected between the investigated cases. The sinusoidal cases evidence a stronger velocity deficit in the centre of the streak (figure 4*c*). Correspondingly, the above-mentioned narrower profile of the streak is further evidenced at values of s^+ yielding higher values of drag reduction (see table 3).

The conditional averaged wall-normal vorticity profiles (figure 4*d*) show these differences further. In particular, the sinusoidal cases exhibit a much steeper gradient at the centre of the streak, associated with a narrower velocity profile. Differently from the case at a lower Reynolds number, the sinusoidal case also evidences larger values of the peak with respect to the Smooth and RLong cases. Even though the differences between the RS1 and RS2 cases are small, the results seem to suggest an effect of the amplitude of the sinusoidal pattern; nevertheless, a broader parametric space, with more investigated amplitudes a, is needed to support this observation. The results of figures 4(*b*) and 4(*d*) show that the sinusoidal riblets enhance the wall-normal vorticity at the streaks' edges, with corresponding large values of in-plane shear.

Further insights into the effect of the riblet geometry can be evidenced by analysing the p.d.f. of the modulus of the in-plane projection of the velocity gradient, $|\nabla \hat{u}|_{x,z}$, calculated in correspondence of the LSS edges. Figures 5(*a*) and 5(*b*) further support the conclusions that have been drawn when discussing the conditional velocity and vorticity profiles.

The riblet cases at $Re_\theta = 2200$ (figure 5*a*) show a shift towards greater values of the peak of the modulus of the velocity gradient. In particular, the RLong, RS1 and RS2 cases feature an increased probability of $|\nabla \hat{u}|_{x,z} > 0.12$. This suggests that the riblet cases are generally characterized by more intense shear regions; furthermore, the amplitude of the sinusoidal geometry seems to introduce even stronger values of the velocity gradients.

At larger values of the Reynolds number, $Re_\theta = 2900$, the RLong case features a behaviour that closely resembles the Smooth case. Conversely, the p.d.f.s of $|\nabla \hat{u}|_{x,z}$ in the sinusoidal cases are characterized by a shift of the peak towards greater values of $|\nabla \hat{u}|_{x,z}$, in agreement with the larger values of wall-normal vorticity evidenced in figure 4.

https://doi.org/10.1017/jfm.2024.256 Published online by Cambridge University Press

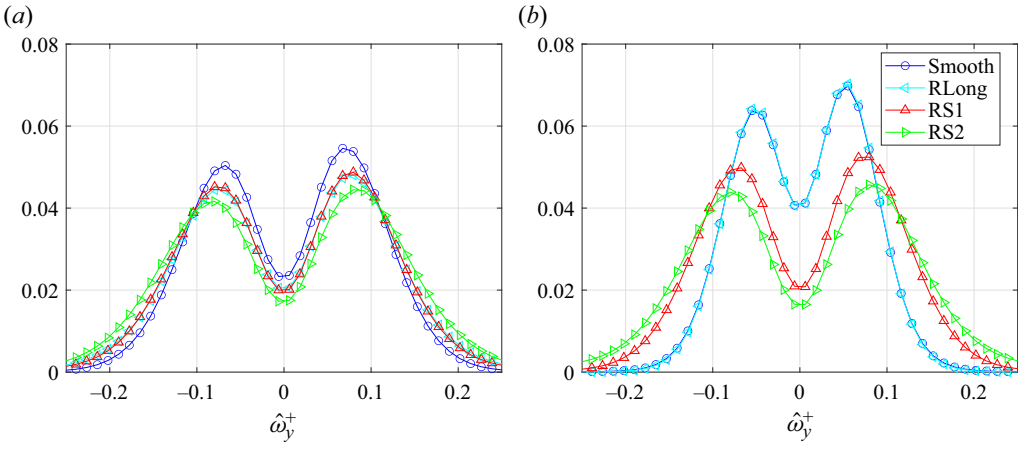


Figure 6. Probability density functions of the wall-normal vorticity $\hat{\omega}_y$ calculated at the streaks' edges. Data are collected at (*a*) $Re_\theta = 2200$ and $y^+ = 35$, (*b*) $Re_\theta = 2900$ and $y^+ = 50$.

The p.d.f. of the conditional wall-normal vorticity calculated at the edges of the LSS is reported figure 6. At $Re_\theta = 2200$, the effect of the riblet geometry is such that smaller values of vorticity become less probable, with a corresponding increment of the probability associated with the tails of the p.d.f., namely for $|\hat{\omega}_y^+| > 0.15$. Correspondingly, the peak of the p.d.f. shows a progressive shift towards larger values of $|\hat{\omega}_y^+|$ when the manipulated cases are considered.

At $Re_\theta = 2900$, the RS cases show a much clearer distinction with respect to both the Smooth and RLong cases. In particular, the RS cases lead to a shift in the maxima of the p.d.f. towards greater values of $|\hat{\omega}_y^+|$. In addition to this, a higher probability of occurrence of values $|\hat{\omega}_y^+| > 0.08$ is detected, with a trend that seems to suggest the effect of the amplitude of the sinusoidal riblet. On the other hand, the RLong case features a p.d.f. of the wall-normal vorticity that closely resembles that of the Smooth case.

Schoppa & Hussain (2002), using transient growth analysis of the streaks, have shown that large values of ω_y are generally associated with streaks that are more prone to instability, and as such give rise to streamwise vortices. In the present case, the greater values of wall-normal vorticity can be responsible not only for the streaks' instability but also for their fragmentation and/or weakening.

Table 4 summarizes the number of educed streaks for each of the investigated cases. In particular, the results are presented in the form of percentage variation with respect to the Smooth case ($\Delta N_S = 100 \times (N_S - N_S^S)/N_S^S$), where N_S indicates the number of streaks in the ribbed cases, and N_S^S the number of educed streaks in the Smooth case. The results seem to suggest that there is a fundamentally different behaviour when comparing the RLong with the RS cases. The latter indeed show a consistent increase in the number of the streaks with respect to the Smooth case. At larger values of the Reynolds number, which correspond to higher effectiveness of the riblets in terms of drag reduction, the number of educed streaks increases.

The results presented in figures 3 and 4, and table 4, allow us to further elaborate on the mechanism by which sinusoidal riblets manipulate the near-wall turbulence. The sinuous geometry leads to streaks that are characterized by larger values of the wall-normal vorticity. This makes the LSS more prone to instability, thus causing their fragmentation.

https://doi.org/10.1017/jfm.2024.256 Published online by Cambridge University Press

Re_θ	RLong	RS1	RS2	y^+
2200	10.6	14.9	19.8	35
2900	−7.0	24.4	31.5	50

Table 4. Percentage variation of the number of educed LSS. The smooth case is taken as a reference.

The fragmentation is reflected in two different aspects: (i) more streaks are educed in the RS cases; (ii) the mean spacing between streaks, as well as their width, is reduced in the RS cases.

Cafiero & Iuso (2022) suggested a possible mechanism leading to the drag reduction evidenced by the sinusoidal riblets, which was associated with the imprint of the geometry manipulation onto the flow field. The spatial periodic inversion triggered by the sinusoidal geometry yields secondary flows and a cross-stream velocity component with an inverted direction at each bend. This mechanism leads to enhanced wall-normal vorticity, along with possible effects on the streamwise and spanwise vorticity that need further analysis in future investigations. The results presented in this paper support the previous hypothesis, linking the fragmentation of the LSS to the spatial variation of vorticity.

A statistical analysis based on two-point correlations of the velocity fluctuations in the wall-parallel (x–z) plane will serve the purpose of elucidating the effects of the wall manipulations on the structure of the LSS.

The two-point correlation between any two quantities A and B is defined as

$$R_{AB}(\Delta x, \Delta z) = \frac{\overline{A(x, z)\, B(x + \Delta x, z + \Delta z)}}{\sigma_A \sigma_B}, \tag{3.1}$$

where σ_A and σ_B are the standard deviations of A and B, respectively, and Δx and Δz are the in-plane separations between the two components. The overbar notation indicates the ensemble average operation over the acquired snapshots. It is worth mentioning that the current analysis is carried out considering that the location at which the correlation is computed is beyond the roughness layer, and as such, homogeneity can be assumed in x and z. Following Cheng *et al.* (2021) and Modesti *et al.* (2021), we estimate the value of the roughness layer as $\delta_r^+ = 0.62 s^+$, which in the most limiting case, $Re_\theta = 2900$, corresponds to $\delta_r^+ = 6.57$.

Figure 7(*a*) shows the two-point correlation R_{uu} calculated at $Re_\theta = 2900$ and $y^+ = 50$, corresponding to the case where the sinusoidal riblets yield the largest values of drag reduction. The contour shows the representative Smooth case, whilst figure 7(*b*) shows the comparison between the four investigated cases for two generic values of the contour line ($R_{uu} = 0.5$ solid line, and $R_{uu} = 0.2$ dashed line) for the four investigated cases.

The Smooth case exhibits iso-lines of the correlation that are elongated in the streamwise direction, which are characteristic of the existence of the low- and high-speed streaks. The RLong case shows a behaviour that is comparable with the Smooth case, with a more elongated correlation lobe, and same width; this result is in good agreement with the data shown in figure 3, which reported values of the streaks' spacing and width that are similar between the Smooth and RLong cases. It is important to point out that the streamwise extent of the iso-lines of correlation is limited by the size of the illuminated region (see § 2). Therefore, it is not surprising if the extent of the correlation map in the streamwise location is sharply interrupted, at least for the Smooth case, in correspondence with $\Delta x^+ \approx 1000$.

https://doi.org/10.1017/jfm.2024.256 Published online by Cambridge University Press

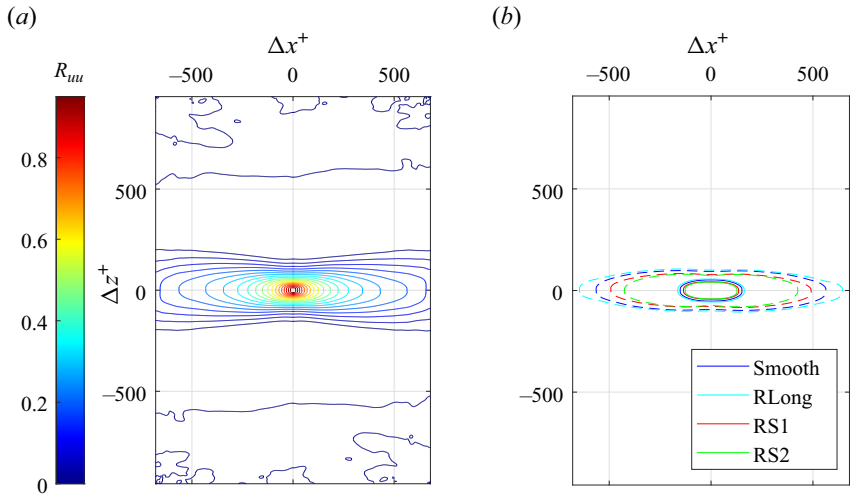


Figure 7. (*a*) Contour plot of the normalized two-point correlations R_{uu} calculated for the Smooth case. (*b*) Comparison between the four investigated cases for two generic contour lines: $R_{uu} = 0.5$ (solid line) $R_{uu} = 0.2$ (dashed line). Data are collected at $Re_\theta = 2900$ and $y^+ = 50$.

	L_x^+	L_z^+
Smooth	334	69
RLong	391	72
RS1	311	60
RS2	249	58

Table 5. Values of the longitudinal (L_x^+) and lateral (L_z^+) integral length scales calculated for the four investigated cases at $Re_\theta = 2900$ and $y^+ = 50$.

The sinusoidal cases show an altered structure of the two-point correlation maps: both the streamwise and spanwise extents of the correlation lobe are indeed reduced. The amplitude of the riblet seems to play a role in how the correlation map is modified: larger values of the amplitude correspond to reduced extents of the correlation maps. This is confirmed quantitatively in table 5, where the values of the streamwise integral length scale (L_x^+) are calculated by integrating the R_{uu} correlation map (figure 7) at $\Delta z^+ = 0$ and reported. In this case, the RLong case yields values of L_x^+ greater than those attained by the Smooth wall (about 17.1 %). On the other hand, both sinusoidal cases feature a reduction in the streamwise extent of the correlation, of 6.9 % and 25.4 % for RS1 and RS2, respectively. A possible explanation for the opposite behaviour between the RLong and RS cases might be associated with a different underlying physics that leads to the drag reduction. The same trend is indeed retrieved also in the values of the spanwise correlation length L_z^+, calculated by integrating the R_{uu} correlation map (figure 7) at $\Delta x^+ = 0$. The effect of the surface manipulation on L_z^+ is quite striking, with the sinusoidal cases featuring a significant reduction. This behaviour is consistent with the manipulation of the near-wall structures by means of the surface geometry, which in turn leads to attenuated and less energetic structures. A possible interpretation for this result can be found in the mechanism leading to the fragmentation of individual structures when manipulated. The

https://doi.org/10.1017/jfm.2024.256 Published online by Cambridge University Press

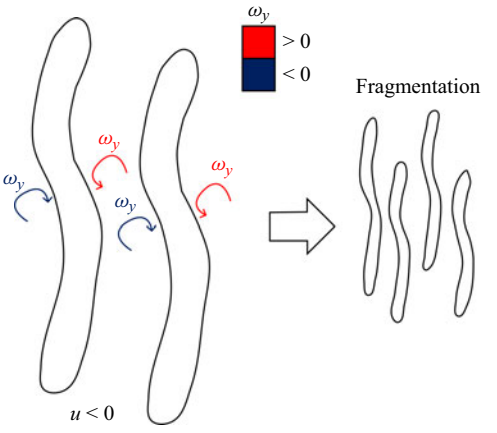


Figure 8. Schematic representation of the fragmentation occurring in the case of sinusoidal manipulation.

effect of the ribbed surface is indeed such that LSS are weakened and, as already pointed out when discussing the p.d.f. of the streaks' spacing (λ_z^+), brought closer together. This is associated with the reduced values of L_z^+. This mechanism is represented schematically in figure 8.

The effect of the sinusoidal geometry on the structure of the turbulent boundary layer is further confirmed by the analysis of the R_{uw} correlation maps (figure 9). The contour plot shows two lobes of correlation of opposite sign, located on either side of $\Delta z^+ = 0$. The positive (negative) correlation lobe is located at $\Delta z^+ > 0$ (< 0). For the representative condition of LSS ($u < 0$), the positive lobe of correlation corresponds to a negative spanwise velocity ($w < 0$), i.e. an entrainment towards the centre of the streak. An opposite behaviour can be envisaged instead for the negative correlation lobe. The distance between the two peaks indicates a measure of the streaks' width. The results are indeed consistent with the description: the spanwise extent of the correlation lobe reduces for the manipulated cases, with RS2 attaining the smallest size.

3.2. *The VISA conditional averages*

The confirmation of the fragmentation mechanism can be sought in the conditional averages calculated across the edges of the low- and high-speed streaks. The edges of the streaks are characterized by strong velocity gradients in the streamwise and spanwise directions, and they are generally associated with values of the local variance of the velocity that are greater than the variance calculated over the entire dataset. When the latter condition is verified, an event is identified.

The approach that has been followed is based on VISA (Johansson, Alfredsson & Kim 1991), which represents the spatial counterpart of the variable interval temporal average (VITA) (Blackwelder & Kaplan 1976). Each instantaneous image is divided into a structured grid. The size of each cell of the grid is then defined, and for the present investigation, a streamwise extent $\Delta\tilde{x}^+ = 200$ and spanwise extent $\Delta\tilde{z}^+ = 100$ have been considered, corresponding to numbers of grid points n_x and n_z in the streamwise and spanwise directions, respectively. At each index (i, j) of the grid, the value of the local

https://doi.org/10.1017/jfm.2024.256 Published online by Cambridge University Press

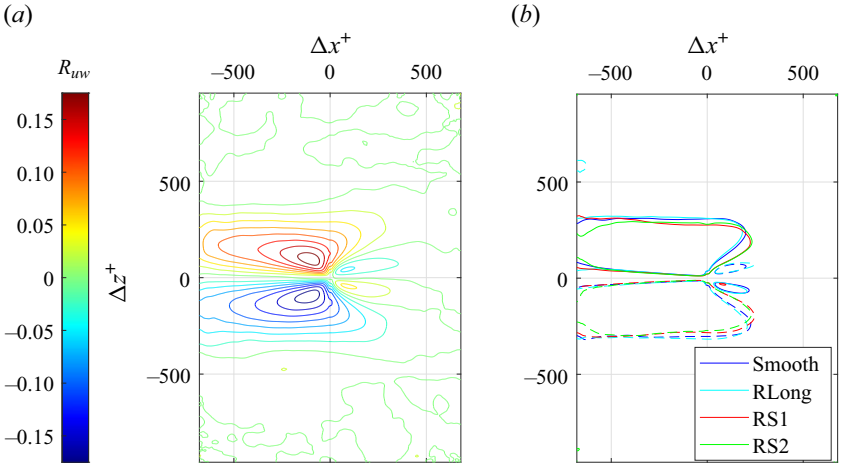


Figure 9. (*a*) Contour plot of the normalized two-point correlations R_{uw} calculated for the Smooth case. (*b*) Comparison between the four investigated cases for one generic contour line, $R_{uw} = \pm 0.04$ (solid/dashed line, respectively). Data are collected at $Re_\theta = 2900$ and $y^+ = 50$.

variance of the streamwise velocity is computed as

$$\overline{u^2}^+_{loc} = \frac{1}{n_x n_z} \sum_{i=1}^{n_x} \sum_{j=1}^{n_z} (u^+(i,j))^2 - \left(\frac{1}{n_x n_z} \sum_{i=1}^{n_x} \sum_{j=1}^{n_z} u^+(i,j) \right)^2, \tag{3.2}$$

where $\overline{u^2}^+_{loc}$ indicates a local average, calculated over the cell of extent $\Delta\tilde{x}^+$, $\Delta\tilde{z}^+$. For each instantaneous image, a corresponding map of the local variance is obtained. Locally, the points that are characterized by values of the local variance $\overline{u^2}^+_{loc}$ greater than k times the global variance $\overline{u^2}^+$ (i.e. calculated over all the snapshots) are identified as VISA events:

$$\overline{u^2}^+_{loc} > k\,\overline{u^2}^+. \tag{3.3}$$

For the present investigation, k has been set to 1.

Di Cicca *et al.* (2002*a*) argued that the VISA events that satisfy the condition of (3.3) are generally found at the edges of the streaks since those regions are characterized by large values of intermittency. Figure 10 shows a representative instantaneous realization of the flow field with overlaid locations of the VISA events. The locations of the events indeed correspond to the regions of intense shear at the edges of the streaks.

Among all the identified events, further conditioning is then applied. In particular, the VISA events that are characterized by $\partial u/\partial x < 0$ and $\partial u/\partial z > 0$ are selected. The selection of these events is purely arbitrary; indeed, by combining the streamwise and cross-stream derivatives of the streamwise velocity component, it is possible to reconstruct all the flanks of a sinuous streak.

Each of the identified events is then averaged considering a window centred on the event location, of extent $\Delta\tilde{x}^+$ in the streamwise direction and $\Delta\tilde{z}^+$ in the cross-stream direction. Figure 11 shows the averaged VISA event of the cross-stream velocity component obtained for the Smooth, RLong, RS1 and RS2 cases with overlaid streamlines. The source of the streamlines is the same for all cases.

https://doi.org/10.1017/jfm.2024.256 Published online by Cambridge University Press

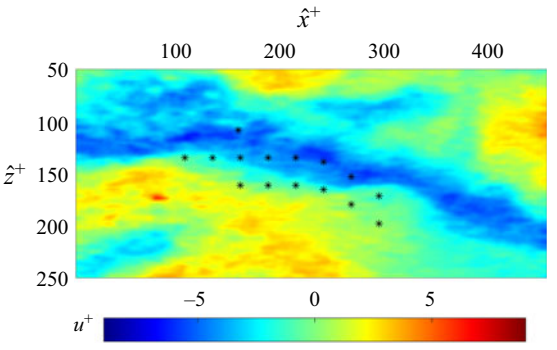


Figure 10. The VISA events detected on a representative instantaneous realization of the flow field overlaid on the colour map of the streamwise velocity fluctuation.

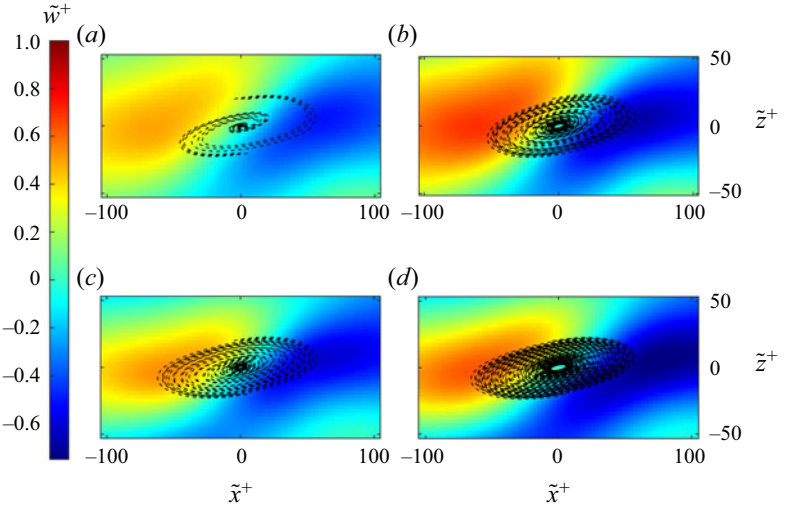


Figure 11. VISA conditionally averaged spanwise velocity ($\tilde{w}^+$) for events characterized by $\partial u/\partial x < 0$ and $\partial u/\partial z > 0$, with overlaid streamlines, for cases (*a*) Smooth, (*b*) RLong, (*c*) RS1, and (*d*) RS2. Data are collected at $Re_\theta = 2900$ and $y^+ = 50$.

Here and in the following, a tilde will be used to indicate VISA quantities. In all cases, the contour shows a region of intense shear, with values of $\tilde{w}^+$ that change in sign when passing from $\tilde{x}^+ < 0$ to $\tilde{x}^+ > 0$, or similarly from $\tilde{z}^+ < 0$ to $\tilde{z}^+ > 0$. This leads to the consideration that the centre of the event is a region of the flow where the streamlines roll up, hence leading to large values of the wall-normal vorticity. Further to this, it can be argued that the manipulated cases show streamlines that are denser than the Smooth case, which can be addressed directly to the larger values of the wall-normal vorticity.

The VISA conditioned profiles of the streamwise ($\tilde{u}^+$) and cross-stream ($\tilde{w}^+$) velocity components extracted at $\tilde{z}^+ = 0$ are reported in figures 12(*a*,*b*). As could also be inferred from the contour plots in figure 4, the effect of the manipulation is such that the ribbed geometry leads to a less intense gradient of the streamwise velocity component compared with the Smooth case. On the other hand, there is no significant difference among the manipulated cases. The cross-stream VISA profiles measured in the streamwise direction show instead an opposite trend with respect to those of figure 12(*a*). All the ribbed cases

https://doi.org/10.1017/jfm.2024.256 Published online by Cambridge University Press

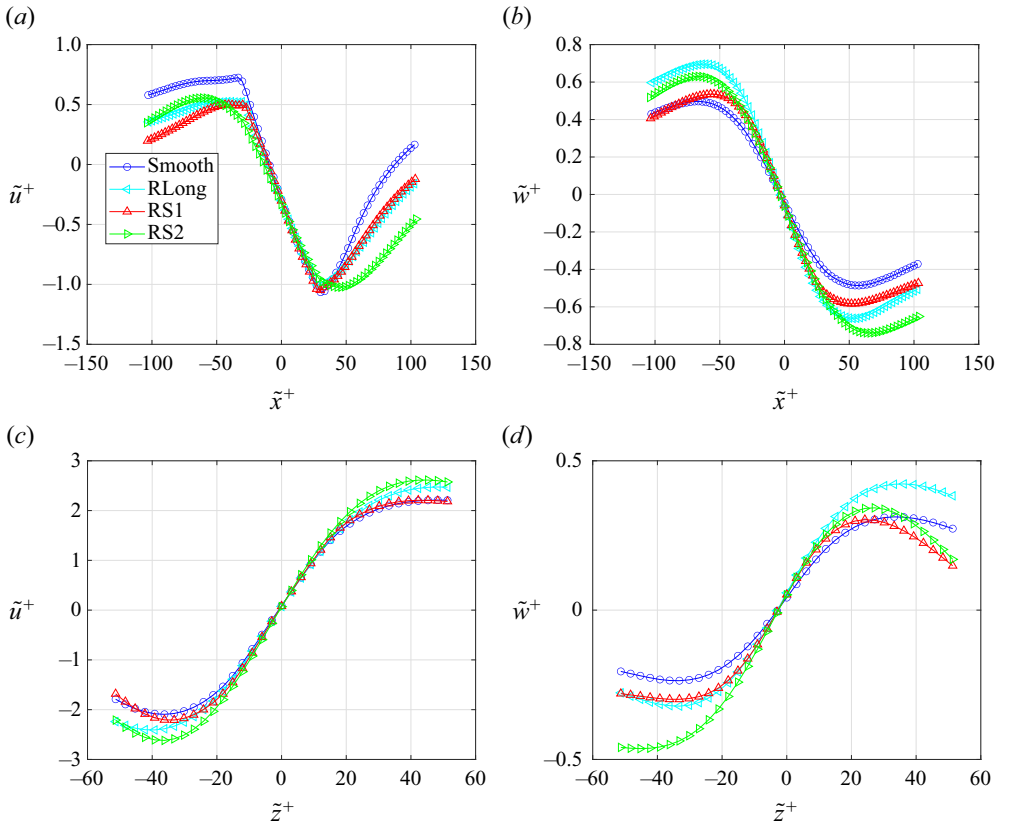


Figure 12. The VISA conditionally averaged streamwise ($\tilde{u}^+$) and spanwise ($\tilde{w}^+$) velocity profiles extracted at (*a*,*b*) $z^+ = 0$ and (*c*,*d*) $x^+ = 0$ for VISA events characterized by $\partial u/\partial x < 0$ and $\partial u/\partial z > 0$, with overlaid streamlines. Data are collected at $Re_\theta = 2900$ and $y^+ = 50$.

display an enhancement of the peak-to-peak value of $\tilde{w}^+$, with the longitudinal case featuring the largest values. This result seems to be at odds with results reported in § 3.1, when describing the effect of the sinusoidal riblets on the wall-normal vorticity. However, the leading term associated with the wall-normal vorticity is $(\partial\tilde{u}/\partial z)^+$, with $(\partial\tilde{w}/\partial x)^+$ being instead significantly smaller.

To confirm that the results are indeed consistent, we show the joint p.d.f. of the velocity gradients $(\partial\tilde{u}/\partial z)^+$, $(\partial\tilde{u}/\partial x)^+$ calculated for the identified events in figure 13(*a*). In particular, the spanwise gradient is linked to the wall-normal vorticity, while the streamwise one relates to the most energetic VISA events. The manipulated cases are characterized by greater velocity gradients $(\partial\tilde{u}/\partial z)^+$ in the spanwise direction, with a corresponding attenuation of the streamwise velocity gradient $(\partial\tilde{u}/\partial x)^+$. This is identified more clearly in figure 13(*b*). Indeed, consistently with the larger values of wall-normal vorticity evidenced at the streak edges by the RS cases, the p.d.f. shows that despite the similarity between the manipulated and Smooth cases, the RS ones yield a higher probability of large values of $(\partial\tilde{u}/\partial z)^+$.

https://doi.org/10.1017/jfm.2024.256 Published online by Cambridge University Press

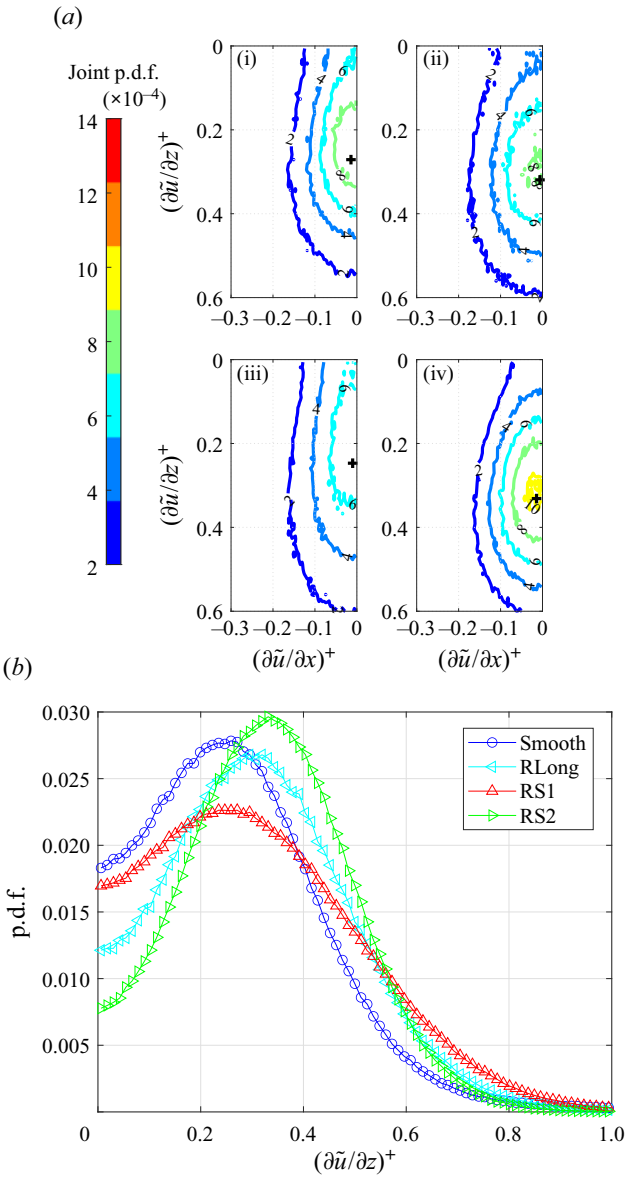


Figure 13. (*a*) Joint p.d.f. of the gradient of the VISA conditioned streamwise velocity calculated along the streamwise ($(\partial\tilde{u}/\partial x)^+$) and cross-stream ($(\partial\tilde{u}/\partial z)^+$) directions at the centre of each VISA event for the (i) Smooth, (ii) RLong, (iii) RS1 and (iv) RS2 cases. (*b*) Marginal p.d.f. of $(\partial\tilde{u}/\partial z)^+$. Data are collected at $Re_\theta = 2900$ and $y^+ = 50$.

3.3. *The VISA conditioned turbulent kinetic energy budget*

The identification of the VISA events is further exploited to elucidate the contribution of the LSS to the production term of the turbulent kinetic energy equation. The planar PIV available for the current experiments provides us access to only some of the terms involved

https://doi.org/10.1017/jfm.2024.256 Published online by Cambridge University Press

in the turbulent kinetic energy budget, which can be formulated as follows:

$$\underbrace{\frac{\bar{U}_k}{2}\frac{\partial \overline{q^2}}{\partial x_k}}_{\mathcal{A}} = \underbrace{-\overline{u_i' u_j'}\frac{\partial \bar{U}_i}{\partial x_j}}_{\mathcal{P}} - \underbrace{\frac{\partial}{\partial x_k}\left(\frac{\overline{u_k' q^2}}{2} + \frac{\overline{u_k' p}}{\rho}\right)}_{\mathcal{T}} + \underbrace{\frac{\nu}{2}\frac{\partial^2 \overline{q^2}}{\partial x_m^2}}_{\mathcal{D}_v} - \varepsilon, \tag{3.4}$$

with $q^2 = u_i'^2$. Here, $\mathcal{A}$, $\mathcal{P}$ and $\mathcal{T}$ indicate the advection, production and transport of turbulent kinetic energy, while $\mathcal{D}_v$ and ε indicate the viscous diffusion and dissipation due to the fluctuating rate of strain. For the present case, given the value of the Reynolds number, $\mathcal{D}_v$ is deemed to be negligible with respect to ε. The turbulent transport $\mathcal{T}$ is constituted of the triple velocity correlation $\overline{u_k' q^2}$ and the pressure velocity correlation $\overline{u_k' p}$.

The purpose of this subsection is to highlight the effect of the surface manipulation on the production term of the turbulent kinetic energy equation. The analysis is carried out on the detected VISA events, in order to focus on how the production and transport are affected by the surface manipulation, limited to the streaks' edges. Given the limited spatial resolution, along with the absence of some of the terms measured with the current PIV set-up, it was not possible to provide information about the dissipation term ($\varepsilon = 2\nu(\overline{s_{ij} s_{ij}})$). On the other hand, considering the wall-normal distance at which the measurements are taken, namely $y^+ = 50$, the transport term attains values that are close to zero (Pope 2000) and as such can be not focal for the present investigation.

Figure 14 shows the production term ($\tilde{\mathcal{P}}$) calculated for the Smooth, RLong, RS1 and RS2 cases from the VISA conditioned flow field, overlaid with the iso-lines of $\tilde{u}^+ = \pm 0.5$. The effect of the surface manipulation is immediately visible in the distribution of the production term. In particular, the introduction of the ribbed surface leads to the attenuation of the production term, regarding both positive and negative terms. All the cases are characterized by two intense lobes, mostly contained within the streak. The identified iso-lines are indeed representative of the shear region between a low-speed streak and a high-speed streak: given the specific conditioning that is considered for the VISA events, which takes into account those events that are characterized by $\partial u/\partial z > 0$ and $\partial u/\partial x < 0$, values $\tilde{z}^+ > 0$ correspond to locations that are outside the LSS. Values $\tilde{z}^+ = 0$, i.e. the centre of the VISA events, are indeed associated with the streaks' edge.

The analysis of the individual terms contributing to the turbulence production, reported here only for the Smooth case for the sake of brevity, shows that the leading term in the turbulence production is $\tilde{\mathcal{P}} \approx \tilde{\mathcal{P}}_{xx} = -\overline{uu}\,\partial\bar{u}/\partial x$, while the remaining three terms (considering the available PIV measurements) are at least one order of magnitude smaller. It must be noted explicitly that the investigated plane neglects the production term that is associated with the strongest component of shear ($\partial\bar{u}/\partial y$) and shear stress ($\overline{uv}$).

The attenuation of the turbulence production in the wall-parallel plane can be ascribed to the already highlighted fragmentation of the near-wall LSS, in the cases of the sinusoidal riblets. In particular, as evidenced in figure 14(*a*), the Smooth case yields intense regions of positive/negative production at the streak boundaries, associated with the more intense streamwise and cross-stream shear rates in the conditional VISA events of figure 12.

All the riblet cases (figures 14*b–d*) are characterized by an attenuation of the turbulence production (both positive and negative). It is interesting to notice how despite there being only small differences between the longitudinal and sinusoidal cases, RLong (figure 14*b*) features a more intense protrusion of the turbulence production within the core of the LSS, i.e. towards $z^+ < 0$ with respect to RS1 (figure 14*c*) and RS2 (figure 14*d*). Indeed, the latter cases are characterized by values of the turbulence production mostly confined

https://doi.org/10.1017/jfm.2024.256 Published online by Cambridge University Press

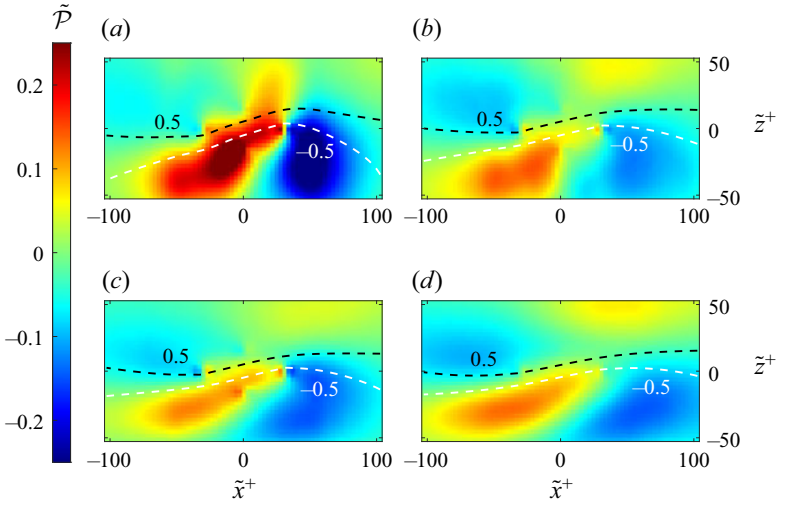


Figure 14. Colour map of the VISA conditionally averaged production ($\tilde{\mathcal{P}}$), overlaid with the isolines $\tilde{u}^+ = \pm 0.5$, for the (*a*) Smooth, (*b*) RLong, (*c*) RS1 and (*d*) RS2 cases. Data are collected at $Re_\theta = 2900$ and $y^+ = 50$.

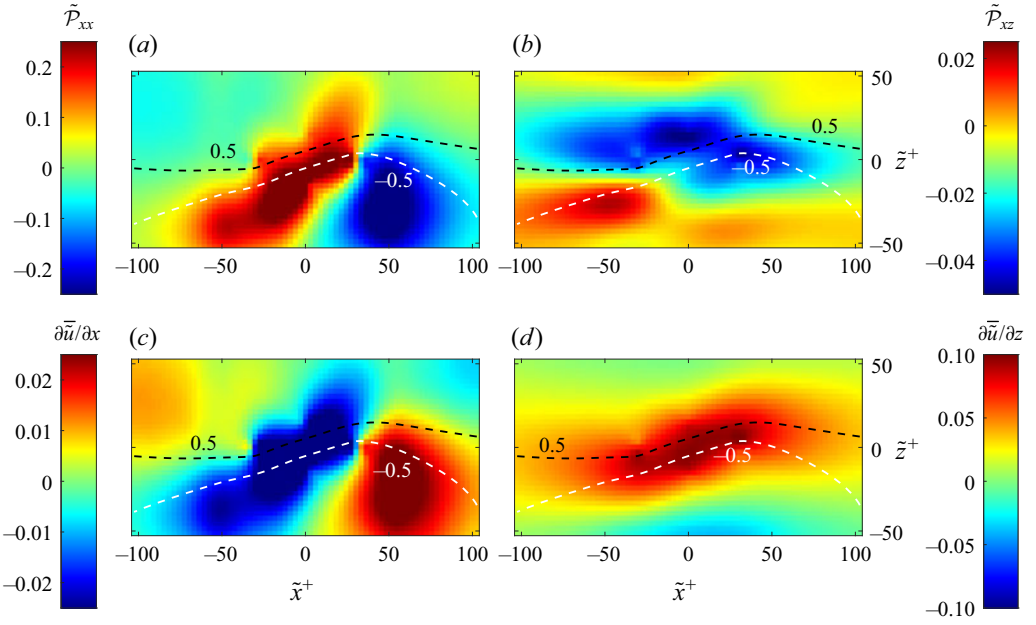


Figure 15. Colour maps of the components of the turbulence production (*a*) $\tilde{\mathcal{P}}_{xx}$ and (*b*) $\tilde{\mathcal{P}}_{xz}$, and corresponding components of the velocity gradient (*c*) $\partial\bar{\tilde{u}}/\partial x$ and (*d*) $\partial\bar{\tilde{u}}/\partial z$ calculated over the VISA events, overlaid with the isolines $\tilde{u}^+ = \pm 0.5$.

at the edges of the streaks (i.e. the centre of the VISA event). This is also in line with the general observation of narrower streaks as highlighted in all the sinusoidal cases.

For one representative condition only, namely the Smooth case, figure 15 shows the comparison between the production terms associated with the normal $\overline{\tilde{u}\tilde{u}}$ and shear $\overline{\tilde{u}\tilde{w}}$ stresses. In particular, figures 15(*a*,*b*) are representative of the $\tilde{\mathcal{P}}_{xx}$ and $\tilde{\mathcal{P}}_{xz}$ terms,

https://doi.org/10.1017/jfm.2024.256 Published online by Cambridge University Press

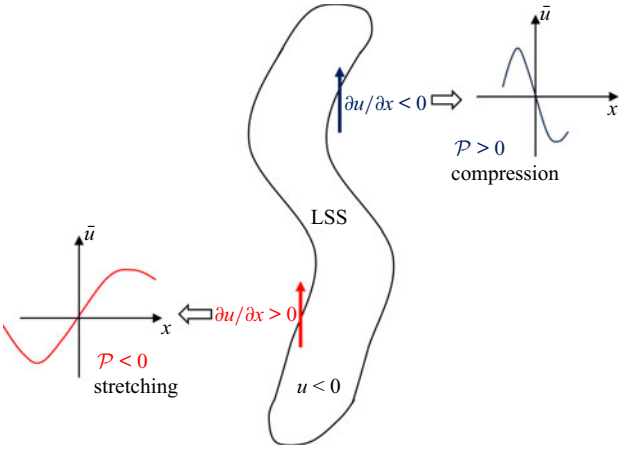


Figure 16. Schematic representation of the relation between the velocity gradient and the values of the turbulence production.

respectively, and figures 15(*c*,*d*) give the associated values of the mean velocity gradients $\partial\bar{\tilde{u}}/\partial x$ and $\partial\bar{\tilde{u}}/\partial z$, respectively. The first immediate conclusion is that the term $\tilde{\mathcal{P}}_{xx}$ is at least one order of magnitude greater than $\tilde{\mathcal{P}}_{xz}$. This is due to the fact that despite the term $\partial\bar{\tilde{u}}/\partial z$ being greater than $\partial\bar{\tilde{u}}/\partial x$, the stress term $\overline{\tilde{u}\tilde{w}}$ attains values close to zero, for all the investigated cases. Conversely, the normal stress term $\overline{\tilde{u}\tilde{u}}$ counterbalances the smaller values of the velocity gradient $\partial\bar{\tilde{u}}/\partial x$, thus yielding greater production values. The comparison of the total production reported in figures 14 and 15 also shows that the regions of negative/positive production are determined mostly by the sign of $\partial\bar{\tilde{u}}/\partial x$. Considering the specific case of VISA events, the regions of negative production are ascribed, for example, to regions of the flow located at the boundaries between LSS and the surrounding flow. Indeed, when a fluid particle moves from the inner to the outer part of LSS, we have the local value $\partial\bar{\tilde{u}}/\partial x > 0$, with corresponding stretching and negative production (Onorato & Iuso 2001). An opposite consideration can be made for the regions of the flow characterized by $\partial\bar{\tilde{u}}/\partial x < 0$, which yield $\tilde{\mathcal{P}} > 0$. This mechanism is also represented schematically in figure 16. It is noteworthy that $\mathcal{P}_{xx}$ is the leading term within the data accessible to the current PIV set-up. Figure 17 reports the turbulence production measured in the wall-normal (x–y) plane from previous experimental campaigns, at the same value of the Reynolds number, $Re_\theta = 2900$. In this case, no conditional averages are applied to the data, thus being indicative of the full components of the Reynolds stresses and shear rates. The leading term is the one related to the wall-normal shear rate, $P_{xy} = -\overline{uv}\,\partial\bar{u}/\partial y$.

The data show that all the surface manipulations lead to an attenuation of the turbulence production, which is particularly significant for values $12 < y^+ < 70$. On the other hand, the differences evidenced between the ribbed surfaces are quite limited, with the RS1 case showing slightly smaller values than RLong and RS2, which could be considered to be within the uncertainty of the measurements.

4. Conclusion

In this paper, we analyse the effect of wall manipulation using sinusoidal riblets on the near-wall structures in a turbulent boundary layer. Wall-parallel particle image velocimetry

https://doi.org/10.1017/jfm.2024.256 Published online by Cambridge University Press

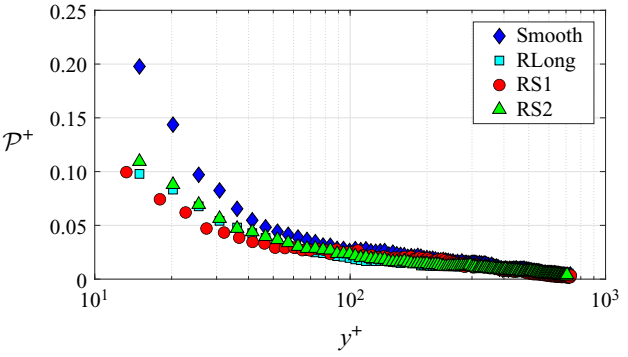


Figure 17. Turbulence production normalized in inner units calculated in the wall-normal plane at $Re_\theta = 2900$. The data are extracted from the dataset of Cafiero & Iuso (2022).

experiments at two different values of the Reynolds number ($Re_\theta = 2200$ and 2900) allow us to carry out conditional averages to characterize the effect of different wall manipulations on low-speed streaks (LSS) and on the VISA events. The analysis reveals that when the sinusoidal riblets cases have efficiency similar to the RLong case in reducing drag ($s^+ = 7.06$), all the investigated cases feature a similar trend of the conditional streamwise velocity and wall-normal vorticity. Conversely, at $Re_\theta = 2900$, corresponding to the value of s^+ yielding the largest drag reduction values ($s^+ = 10.6$), the conditionally averaged velocity profiles of the educed LSS depart significantly from the Smooth case when the sinusoidal manipulation is considered. Namely, the streaks profile becomes narrower, with corresponding larger values of the wall-normal vorticity. This behaviour is not evidenced in the RLong case, which follows a trend similar to the Smooth case, thus suggesting that the drag reduction mechanism of the RS cases is inherently different with respect to the RLong case.

The statistical description of the LSS also shows that the RS cases lead to their fragmentation at $Re_\theta = 2900$, with a corresponding substantial increment of their number (about 24 % in RS1 and 31.5 % in RS2, respectively) compared to the Smooth case, which agrees with the reduced spacing λ_z^+ between LSS. This is further confirmed by the two-point correlation analysis, which highlights how in the case $Re_\theta = 2900$, the RS cases lead to a substantial effect on the streamwise correlation and, even more significantly, the cross-stream correlation.

The fragmentation of the LSS occurring under the sinusoidal manipulation can be attributed to the periodic transversal flow generated by the sinuous grooves. In fact, the periodic spanwise flow inversion not only modifies the wall-normal vorticity, as shown extensively in this paper, but is also expected to tamper with the streamwise and spanwise vorticity components. The manipulation mechanism of the near-wall flow associated with the sinusoidal riblets seems to add further complexity to the widely accepted wall-normal displacement of the near-wall structures that characterizes the longitudinal grooves. Further investigations are ongoing to confirm these points, but there seems to be enough evidence in support of the effect of the amplitude on how the ribbed geometry manipulates the turbulent structures: the structures appear to be weakened, yet retaining an ordered structure.

Therefore, it could be argued that the effects introduced by the sinusoidal riblets resemble those of the spanwise wall oscillation, although in a much less significant fashion, the latter being an active flow manipulation.

https://doi.org/10.1017/jfm.2024.256 Published online by Cambridge University Press

The VISA conditional averages allowed us to describe the behaviour at the streak boundaries. We performed conditional averages to identify those events that correspond to $\partial u/\partial x < 0$ and $\partial u/\partial z > 0$, which is one representative flank of a streak. In the streamwise direction, VISA events are less intense, with a corresponding enhancement of the intensity in the cross-stream direction, which can be associated with the induced spanwise oscillation induced by the riblet geometry. This is particularly visible from the p.d.f. of $\partial u/\partial z$, which shows that a higher probability of larger spanwise gradients is associated with the sinusoidal manipulation.

The analysis of the turbulence production term applied to the VISA events reveals an attenuation for all the manipulated cases with respect to the Smooth case. In the RS cases, the turbulence production is mostly limited to the streaks' edges, where the shear rates are significantly greater. Conversely, the Smooth and RLong cases show a more intense contribution to the turbulence production from the core of the streaks.

Acknowledgements. The authors wish to thank Professor T. Astarita for providing the software used to acquire and process the PIV images, and acknowledge F. Casagrande, S. Saggiomo and G. Virgillito for their help during the experiments.

Funding. The project has received funding from the Clean Sky 2 Joint Undertaking under the European Union's Horizon 2020 research and innovation program under grant agreement no. 945548 - GAM-2020-REG, and it was carried out within the GREENER project – funded by the European Union – Next Generation EU within the PRIN 2022 program (D.D. 104 - 02/02/2022 Ministero dell'Universit'a e della Ricerca). This paper reflects only the authors' views and opinions, and the Ministry cannot be considered responsible for them.

Declaration of interests. The authors report no conflict of interest.

Author ORCIDs.
Gioacchino Cafiero https://orcid.org/0000-0003-1251-4802;
Enrico Amico https://orcid.org/0000-0003-4902-8023;
Gaetano Iuso https://orcid.org/0000-0002-8132-4124.

References

Adrian, R.J., Meinhart, C.D. & Tomkins, C.D. 2000 Vortex organization in the outer region of the turbulent boundary layer. *J. Fluid Mech.* **422**, 1–54.

Astarita, T. 2006 Analysis of interpolation schemes for image deformation methods in PIV: effect of noise on the accuracy and spatial resolution. *Exp. Fluids* **40** (6), 977–987.

Astarita, T. 2007 Analysis of weighting windows for image deformation methods in PIV. *Exp. Fluids* **43** (6), 859–872.

Astarita, T. 2008 Analysis of velocity interpolation schemes for image deformation methods in PIV. *Exp. Fluids* **45** (2), 257–266.

Bechert, D.W., Bruse, M., Hage, W., Van Der Hoeven, J.G.T. & Hoppe, G. 1997 Experiments on drag-reducing surfaces and their optimization with an adjustable geometry. *J. Fluid Mech.* **338**, 59–87.

Blackwelder, R.F. & Kaplan, R.E. 1976 On the wall structure of the turbulent boundary layer. *J. Fluid Mech.* **76** (1), 89–112.

Cafiero, G., Castrillo, G. & Astarita, T. 2021 Turbulence properties in jets with fractal grid turbulence. *J. Fluid Mech.* **915**, A12.

Cafiero, G., Castrillo, G., Greco, C.S. & Astarita, T. 2019 On the effects of square-fractal turbulators on the flow field generated by a synthetic jet actuator. *Exp. Therm. Fluid Sci.* **102**, 302–315.

Cafiero, G. & Iuso, G. 2022 Drag reduction in a turbulent boundary layer with sinusoidal riblets. *Exp. Therm. Fluid Sci.* **139**, 110723.

Cannata, M., Cafiero, G. & Iuso, G. 2020 Large-scale forcing of a turbulent channel flow through spanwise synthetic jets. *AIAA J.* **58** (5), 2042–2052.

Chan, I.C., Örlü, R., Schlatter, P. & Chin, R.C. 2021 The skin-friction coefficient of a turbulent boundary layer modified by a large-eddy break-up device. *Phys. Fluids* **33** (3), 035153.

https://doi.org/10.1017/jfm.2024.256 Published online by Cambridge University Press

CHANDRAN, D., ZAMPIRON, A., ROUHI, A., FU, M.K., WINE, D., HOLLOWAY, B., SMITS, A.J. & MARUSIC, I. 2023 Turbulent drag reduction by spanwise wall forcing. Part 2. High-Reynolds-number experiments. *J. Fluid Mech.* **968**, A7.

CHENG, X.Q., WONG, C.W., HUSSAIN, F., SCHRÖDER, W. & ZHOU, Y. 2021 Flat plate drag reduction using plasma-generated streamwise vortices. *J. Fluid Mech.* **918**, A24.

CHOI, H., MOIN, P. & KIM, J. 1993 Direct numerical simulation of turbulent flow over riblets. *J. Fluid Mech.* **255**, 503–539.

CHOI, K.S. 1989 Near-wall structure of a turbulent boundary layer with riblets. *J. Fluid Mech.* **208**, 417–458.

CHOI, K.S. 2002 Near-wall structure of turbulent boundary layer with spanwise-wall oscillation. *Phys. Fluids* **14** (7), 2530–2542.

CORKE, T.C. & THOMAS, F.O. 2018 Active and passive turbulent boundary-layer drag reduction. *AIAA J.* **56** (10), 3835–3847.

DI CICCA, G.M., IUSO, G., SPAZZINI, P.G. & ONORATO, M. 2002*a* Particle image velocimetry investigation of a turbulent boundary layer manipulated by spanwise wall oscillations. *J. Fluid Mech.* **467**, 41–56.

DI CICCA, G.M., IUSO, G., SPAZZINI, P.G. & ONORATO, M. 2002*b* PIV study of the influence of large-scale streamwise vortices on a turbulent boundary layer. *Exp. Fluids* **33**, 663–669.

DU, Y., SYMEONIDIS, V. & KARNIADAKIS, G.E. 2002 Drag reduction in wall-bounded turbulence via a transverse travelling wave. *J. Fluid Mech.* **457**, 1–34.

ENDRIKAT, S., MODESTI, D., GARCÍA-MAYORAL, R., HUTCHINS, N. & CHUNG, D. 2021 Influence of riblet shapes on the occurrence of Kelvin–Helmholtz rollers. *J. Fluid Mech.* **913**, A37.

ENDRIKAT, S., NEWTON, R., MODESTI, D., GARCÍA-MAYORAL, R., HUTCHINS, N. & CHUNG, D. 2022 Reorganisation of turbulence by large and spanwise-varying riblets. *J. Fluid Mech.* **952**, A27.

GANAPATHISUBRAMANI, B., LONGMIRE, E.K. & MARUSIC, I. 2003 Characteristics of vortex packets in turbulent boundary layers. *J. Fluid Mech.* **478**, 35–46.

GARCÍA-MAYORAL, R. & JIMÉNEZ, J. 2011 Drag reduction by riblets. *Phil. Trans. R. Soc.* A **369** (1940), 1412–1427.

GARCIA-MAYORAL, R. & JIMENEZ, J. 2012 Scaling of turbulent structures in riblet channels up to $Re_\tau \approx$ 550. *Phys. Fluids* **24** (10), 105101.

GATTI, D. & QUADRIO, M. 2016 Reynolds-number dependence of turbulent skin-friction drag reduction induced by spanwise forcing. *J. Fluid Mech.* **802**, 553–582.

GEHLERT, P., CHERFANE, Z., CAFIERO, G. & VASSILICOS, J.C. 2021 Effect of multiscale endplates on wing-tip vortex. *AIAA J.* **59** (5), 1614–1628.

GRÜNEBERGER, R., KRAMER, F., WASSEN, E., HAGE, W., MEYER, R. & THIELE, F. 2012 Influence of wave-like riblets on turbulent friction drag. In *Nature-Inspired Fluid Mechanics: Results of the DFG Priority Programme 1207 'Nature-inspired Fluid Mechanics' 2006–2012*, pp. 311–329. Springer.

HURST, E., YANG, Q. & CHUNG, Y.M. 2014 The effect of Reynolds number on turbulent drag reduction by streamwise travelling waves. *J. Fluid Mech.* **759**, 28–55.

HUTCHINS, N. & MARUSIC, I. 2007 Evidence of very long meandering features in the logarithmic region of turbulent boundary layers. *J. Fluid Mech.* **579**, 1–28.

IUSO, G., DI CICCA, G.M., ONORATO, M., SPAZZINI, P.G. & MALVANO, R. 2003 Velocity streak structure modifications induced by flow manipulation. *Phys. Fluids* **15**, 2602–2612.

IUSO, G. & ONORATO, M. 1995 Turbulent boundary layer manipulation by outer-layer devices. *Meccanica* **30** (4), 359–376.

IUSO, G., ONORATO, M., SPAZZINI, P.G. & DI CICCA, G.M. 2002 Wall turbulence manipulation by large-scale streamwise vortices. *J. Fluid Mech.* **473** , 23–58.

JIMÉNEZ, J. 2022 The streaks of wall-bounded turbulence need not be long. *J. Fluid Mech.* **945**, R3.

JIMÉNEZ, J. & PINELLI, A. 1999 The autonomous cycle of near-wall turbulence. *J. Fluid Mech.* **389**, 335–359.

JOHANSSON, A.V., ALFREDSSON, P.H. & KIM, J. 1991 Evolution and dynamics of shear-layer structures in near-wall turbulence. *J. Fluid Mech.* **224**, 579–599.

KLINE, S.J., REYNOLDS, W.C., SCHRAUB, F.A. & RUNSTADLER, P.W. 1967 The structure of turbulent boundary layers. *J. Fluid Mech.* **30**, 741–773.

KRAMER, F., GRUENEBERGER, R., THIELE, F., WASSEN, E., HAGE, W. & MEYER, R. 2010 Wavy riblets for turbulent drag reduction. In *5th Flow Control Conference*, p. 4583. ARC–AIAA.

LIN, J., LAVAL, J.P., FOUCAUT, J.M. & STANISLAS, M. 2008 Quantitative characterization of coherent structures in the buffer layer of near-wall turbulence. Part 1: streaks. *Exp. Fluids* **45** (6), 999–1013.

LU, S.S. & WILLMARTH, W.W. 1973 Measurements of the structure of the Reynolds stress in a turbulent boundary layer. *J. Fluid Mech.* **60**, 481–511.

LUCHINI, P., MANZO, F. & POZZI, A. 1991 Resistance of a grooved surface to parallel flow and cross-flow. *J. Fluid Mech.* **228**, 87–109.

https://doi.org/10.1017/jfm.2024.256 Published online by Cambridge University Press

MALATHI ANANTH, S., NARDINI, M., VAID, A., KOZUL, M., RAO, V.N. & SANDBERG, R.D. 2023 Riblet performance beneath transitional and turbulent boundary layers at low Reynolds numbers. *AIAA J.* **61** (5), 1986–2001.

MAMORI, H., YAMAGUCHI, K., SASAMORI, M., IWAMOTO, K. & MURATA, A. 2019 Dual-plane stereoscopic PIV measurement of vortical structure in turbulent channel flow on sinusoidal riblet surface. *Eur. J. Mech. (*B*/Fluids)* **74**, 99–110.

MARUSIC, I., CHANDRAN, D., ROUHI, A., FU, M.K., WINE, D., HOLLOWAY, B., CHUNG, D. & SMITS, A.J. 2021 An energy-efficient pathway to turbulent drag reduction. *Nat. Commun.* **12** (1), 5805.

MELE, B. & TOGNACCINI, R. 2018 Slip length-based boundary condition for modeling drag reduction devices. *AIAA J.* **56**, 3478–3490.

MELE, B., TOGNACCINI, R., CATALANO, P. & DE ROSA, D. 2020 Effect of body shape on riblets performance. *Phys. Rev. Fluids* **5**, 124609.

MENDEZ, M.A., RAIOLA, M., MASULLO, A., DISCETTI, S., IANIRO, A., THEUNISSEN, R. & BUCHLIN, J.M. 2017 POD-based background removal for particle image velocimetry. *Exp. Therm. Fluid Sci.* **80**, 181–192.

MODESTI, D., ENDRIKAT, S., HUTCHINS, N. & CHUNG, D. 2021 Dispersive stresses in turbulent flow over riblets. *J. Fluid Mech.* **917**, A55.

OKABAYASHI, K. 2016 Direct numerical simulation for modification of sinusoidal riblets. *J. Fluid Sci. Technol.* **11** (3), JFST0015.

ONORATO, M. & IUSO, G. 2001 Probability density function and 'plus' and 'minus' structure functions in a turbulent channel flow. *Phys. Rev.* E **63** (2), 025302.

ORLANDI, P. & JIMÉNEZ, J. 1994 On the generation of turbulent wall friction. *Phys. Fluids* **6** (2), 634–641.

PANTON, R.L. 2001 Overview of the self-sustaining mechanisms of wall turbulence. *Prog. Aerosp. Sci.* **37** (4), 341–383.

PEET, Y. & SAGAUT, P. 2009 Theoretical prediction of turbulent skin friction on geometrically complex surfaces. *Phys. Fluids* **21** (10), 105105:1–19.

PEET, Y., SAGAUT, P. & CHARRON, Y. 2008 Turbulent drag reduction using sinusoidal riblets with triangular cross-section. In *38th AIAA Fluid Dynamics Conference and Exhibit*. ARC–AIAA.

POPE, S.B. 2000 *Turbulent Flows*. Cambridge University Press.

QUADRIO, M. & RICCO, P. 2004 Critical assessment of turbulent drag reduction through spanwise wall oscillations. *J. Fluid Mech.* **521**, 251–271.

RAN, W., ZARE, A. & JOVANOVIĆ, M.R. 2021 Model-based design of riblets for turbulent drag reduction. *J. Fluid Mech.* **906**, A7.

RICCO, P. 2004 Modification of near-wall turbulence due to spanwise wall oscillations. *J. Turbul.* **5** (1), 024.

RICCO, P., SKOTE, N. & LESCHZINER, M.A. 2021 A review of turbulent skin-friction drag reduction by near-wall transverse forcing. *Prog. Aerosp. Sci.* **123**, 100713.

ROUHI, A., ENDRIKAT, S., MODESTI, D., SANDBERG, R.D., ODA, T., TANIMOTO, K., HUTCHINS, N. & CHUNG, D. 2022 Riblet-generated flow mechanisms that lead to local breaking of Reynolds analogy. *J. Fluid Mech.* **951**, A45.

ROUHI, A., FU, M.K., CHANDRAN, D., ZAMPIRON, A., SMITS, A.J. & MARUSIC, I. 2023 Turbulent drag reduction by spanwise wall forcing. Part 1. Large-eddy simulations. *J. Fluid Mech.* **968**, A6.

SASAMORI, M., IIHAMA, O., MAMORI, H., IWAMOTO, K. & MURATA, A. 2017 Parametric study on a sinusoidal riblet for drag reduction by direct numerical simulation. *Flow Turbul. Combust.* **99** (1), 47–69.

SASAMORI, M., IWAMOTO, K. & MURATA, A. 2012 Experimental study on drag-reduction effect of a new sinusoidal riblet. In *Fluids Engineering Division Summer Meeting*, vol. 44755, pp. 945–950. American Society of Mechanical Engineers.

SASAMORI, M., MAMORI, H., IWAMOTO, K. & MURATA, A. 2014 Experimental study on drag-reduction effect due to sinusoidal riblets in turbulent channel flow. *Exp. Fluids* **55** (10), 1828.

SCHOPPA, W. & HUSSAIN, F. 1998 Genesis of longitudinal vortices in near-wall turbulence. *Meccanica* **33**, 489–501.

SCHOPPA, W. & HUSSAIN, F. 2000 Coherent structure dynamics in near-wall turbulence. *Fluid Dyn. Res.* **26** (2), 119.

SCHOPPA, W. & HUSSAIN, F. 2002 Coherent structure generation in near-wall turbulence. *J. Fluid Mech.* **453**, 57–108.

SIROVICH, L. & KARLSSON, S. 1997 Turbulent drag reduction by passive mechanisms. *Nature* **388** (6644), 753–755.

SKOTE, M. 2012 Temporal and spatial transients in turbulent boundary layer flow over an oscillating wall. *Intl J. Heat Fluid Flow* **38**, 1–12.

https://doi.org/10.1017/jfm.2024.256 Published online by Cambridge University Press

SKOTE, M. 2013 Comparison between spatial and temporal wall oscillations in turbulent boundary layer flows. *J. Fluid Mech.* **730**, 273–294.

SKOTE, M. 2014 Scaling of the velocity profile in strongly drag reduced turbulent flows over an oscillating wall. *Intl J. Heat Fluid Flow* **50**, 352–358.

TOUBER, E. & LESCHZINER, M.A. 2012 Near-wall streak modification by spanwise oscillatory wall motion and drag-reduction mechanisms. *J. Fluid Mech.* **693**, 150–200.

VISWANATH, P.R. 2002 Aircraft viscous drag reduction using riblets. *Prog. Aerosp. Sci.* **38** (6-7), 571–600.

VON DEYN, L.H., GATTI, D. & FROHNAPFEL, B. 2022 From drag-reducing riblets to drag-increasing ridges. *J. Fluid Mech.* **951**, A16.

VUKOSLAVCEVIC, P., WALLACE, J.M. & BALINT, J.-L. 1992 Viscous drag reduction using streamwise-aligned riblets. *AIAA J.* **30** (4), 1119–1122.

WALSH, M. 1980 Drag characteristics of V-groove and transverse curvature riblets. In *Viscous Flow Drag Reduction*, pp. 168–184. NASA Technical Reports Server.

WALSH, M. 1982 Turbulent boundary layer drag reduction using riblets. *AIAA J.* **82** (9), 0169.

WALSH, M. 1983 Riblets as a viscous drag reduction technique. *AIAA J.* **21** (4), 485–486.

WONG, J., CAMOBRECO, C.J., GARCÍA-MAYORAL, R., HUTCHINS, N. & CHUNG, D. 2024 A viscous vortex model for predicting the drag reduction of riblet surfaces. *J. Fluid Mech.* **978**, A18.

YAO, J., CHEN, X. & HUSSAIN, F. 2018 Drag control in wall-bounded turbulent flows via spanwise opposed wall-jet forcing. *J. Fluid Mech.* **852**, 678–709.

YAO, J., CHEN, X. & HUSSAIN, F. 2019 Reynolds number effect on drag control via spanwise wall oscillation in turbulent channel flows. *Phys. Fluids* **31** (8), 085108:1–16.

ZHANG, Y., CAI, J. & LI, W. 2024 Direct numerical simulations of the drag degradation mechanism in channel flow over trapezoidal riblets. *Aerosp. Sci. Technol.* **144**, 108821.

ZHOU, J., ADRIAN, R.J., BALACHANDAR, S. & KENDALL, T.M. 1999 Mechanisms for generating coherent packets of hairpin vortices in channel flow. *J. Fluid Mech.* **387**, 353–396.

https://doi.org/10.1017/jfm.2024.256 Published online by Cambridge University Press